Development of positioning systems for an automatic combine harvester

（コンバインハーベスタ自動化のための測位システムに関する研究）

Hokkaido University Graduate School of Agriculture
Frontiers in Production Sciences, Doctor Course

Kannapat Udompant

TABLE OF CONTENTS

Acknowledgement

ACKNOWLEDGMENTS

I would like to express my deep gratitude Dr. Noboru Noguchi, my research supervisor, for his patient guidance, enthusiastic encouragement and useful critiques of this research work.

My grateful thanks are also extended to Dr. Kazunobu Ishii. I would like to thank him for sharing his knowledge and his many helpful advice for my research.

I also would like to extend my thanks to Dr. Hiroshi Okamoto for sharing his knowledge in programming and image processing.

And also, I would like to give my gratitude Dr. Ricardo Ospina Alarcon who always supported with my research and gave many great advice for writing a journal paper.

Furthermore, I would like to express thank to Dr. Nobutaka Ito and Dr. Chaichana Chatchawan who recommended me to study in the Laboratory of Vehicle Robotics, Graduate School Agriculture, Hokkaido University. Without their support, I would not have had the opportunity to study in the top laboratory in the field of robot agricultural vehicles.

Finally, I would like to thank my parents for their love, understanding and support.

LIST OF FIGURES

LIST OF TABLES

NOTATION

$2DRMS$	Twice Distance Root Mean Square
$Bel(A)$	Belief function for hypothesis A
$Bel_{d_j^i}^{s^k}\|2^{\Omega}$	Belief function for a feature
$Bel_{d^i}^{s^k}\|2^{\Phi}$	Belief function for a description
$Bel_{p}^{d^i s^k}\|2^{\Theta}$	Belief function for a percept
CEP	Circular Error Probability
Con	The weight of conflict metric
H	Height of the laser rangefinder
$Pl(A)$	Plausibility function for hypothesis A
d	The transverse distance of the RGB camera to the center of origin on the xy plane
h_c	The height of the camera from the ground
l	The longitudinal distance of the RGB camera to the center of origin on the xy plane
$m(A_i)$	Probability mass of a proposition A_i

$m * n$	The image resolution
$r_{d_j^i}$	Description interpretation enlargement function
r_p	Percept interpretation enlargement function
$RMSE$	Root Mean Square Error
u_{opt}	Optimum demarcation of two classes
u^*	The separation of two classes
x	The position in the vehicle's Cartesian coordinates system in x axis
y	The position in the vehicle's Cartesian coordinates system in y axis
z	The position in the vehicle's Cartesian coordinates system in z axis
x_L	The position in the laser rangefinder coordinate system in x axis
y_L	The position in the laser rangefinder coordinate system in y axis
Θ	Frame of discernment
α	The half of angular aperture
$\bar{\gamma}$	The yaw angle of the RGB camera
$\varepsilon_{d_j^i}^{s^k}$	The evidence for a feature
$\varepsilon_{d^i}^{s^k}$	The evidence for a description

Notation

ε_p	The evidence for a percept
θ	The pitch angle of the RGB camera
θ_L	Angle between the x_L axis and the beam direction
θ_p	Angle in pitch direction collected by IMU
θ_r	Angle on roll direction collected by IMU
μ	Mean of the two classes
μ_1	Mean of class 1
μ_2	Mean of class 2
ρ	Distance between the reference origin and the object's detected point
σ_B^2	Between-class variance
σ_w^2	Intra-class variance
$\emptyset$	The null set

ACRONYMS AND ABBREVIATIONS

2D	Two-Dimensional
3D	Three-Dimensional
ALDCBS	Amplified Loaded DC Blocked Splitter
CLAS	Centimeter Level Augmentation Service
CMAS	Centimeter-Class Augmentation System
CORS	Continuously Operation Reference Stations
CG	Center of Gravity
IMU	Inertial Measurement Unit
IPM	Inverse Perspective Mapping
ISP	Internet Service Provider
JAXA	Japan Aerospace Exploration Agency
FDS	Fulltime Drive System
GLONASS	Global’naya Navigasionnaya Sputnikovaya Sistema
GPS	Global Positioning System
GNSS	Global Navigation Satellite System
LEX	L-band Experiment

MADOCA	Multi-Global Navigation Satellite System Advanced Demonstration tool for Orbit and Clack Analysis
MCS	Master Control Station
MP	Megapixels
MS	Monitoring Station
PC	Personal Computer
PNT	Positioning, Navigation, and Timing
PPP	Precise Point Positioning
PTO	Power take-off
PTU	Pan tilt unit
RMSE	Root-mean-square error
ROI	Region of Interest
RTK	Real-Time Kinematic
SFX	Sensor fusion effect
SSR	State Space Representation
TCS	Tracking Control Stations
TOF	Time of Flight

UTM	Universal Transverse Mercator
VRS	Virtual Reference Station
QZO	Quasi-Zenith Orbit
QZSs	Quasi-Zenith Navigation Satellites
QZSS	Quasi-Zenith Satellite System

CHAPTER 1
INTRODUCTION

This chapter presents the concepts of an agricultural automatic vehicle. It shows that the automatic agricultural vehicle can be a proficient counteraction for the worldwide agricultural problems. It also introduces the motivation of this research and the objectives of the research.

1.1 Research background

Nowadays, the problem of food shortage is a great urgency all around the world caused by the population growth. Furthermore, agricultural production confronts the issue of the decreasing of agricultural labor, especially in developed countries.

Therefore, in modern agriculture, many researchers are interested in a positioning system or a navigation system for agricultural vehicles. From the literature review, many motivations are evident from spending of endeavor towards the development of positioning systems for an automatic vehicle, either fully automatic or partially automatic. The development of positioning systems has been stimulated by the rapid development in electronics, computers, and computing technologies. Positioning information of the vehicle is provided by any positioning technology, referenced either in a global coordinate system or in a local coordinate system

1.1.1 Agricultural automatic vehicle

The driver of an agricultural vehicle requires a high concentration while driving either straight or parallel to a certain curve. Additionally, the driver also needs to pay attention to the safe driving. Therefore, the driver’s fatigue is possible to happen caused by the above

mentioned factors. However, the mentioned issue can be solved by utilization of an automatic agricultural vehicle. Because a robot never lacks concentration.

The technological development of the global economy in the defense and transportation sectors often establish trends in the development and evolution of agricultural machineries. A fundamental role in increasing the efficiency and cost reduction of industrial production have been played by robots. For the agricultural sector, Global Navigation Satellite System (GNSS) - and machine vision- based self-guided tractors and harvesters have already been available commercially in the past twenty years. To counteract with the aging population and labor force reduction issue, the agricultural industry must increase productivity, reduce production cost, and improve the quality of agricultural products. These future agricultural productions needs can be achieved by the robotics and automations.

Figure 1.1 shows a wheel type-robot tractor developed by the Vehicle Robotics Laboratory (VeBots) of Hokkaido University in Japan. Many farm works like seeding, tillage, cultivation, etc. could be done automatically. A robot controller fixed inside the tractor can control the steering, engine rotation, vehicle speed, Power take-off (PTO), and hitch.

Figure 1.1 A robot tractor developed by VeBots Lab. in Japan.

In general, automatic agricultural vehicles are classified into two categories: used for open fields and used for indoors. The vehicles used for open fields category are usually applied to harvesting, tillage, fertilizing, spraying, cultivating, and transportation (Chateau et al., 2000; Bell, 1999; Fehr et al., 1995; Noguchi, 1998; Reid & Searcy, 1987; Stombaugh et al., 1998). Orchard vehicles are also included into this category. However, they should be treated in a different way because the environment in the orchard is different from a paddy field or wheat field. The GNSS signals are usually blocked by the canopy in the orchard (Barawid et al., 2007). For the vehicles used for indoors category, are mainly involved in greenhouse works. The machines in this category are navigated mainly using the machine vision and dead reckoning techniques rather than GNSS (Yin et al., 2013).

1.1.2 Positioning system for an automatic combine harvester

Positioning systems have been designed to accomplish automated navigation on agricultural vehicle since a hundred years ago i.e., furrows were used for tractors navigation across fields to reduce endeavor from the operator since 1920s. Technology and innovation have been improved since that time. These improvements influenced the evolution of automated guidance from mechanical sensing to electronic sensors, machine vision, and GNSS to successfully navigate vehicles following parallel paths through the field. A straight line from starting point to ending point is input into the control console of the vehicle, and the GNSS coordinates are collected at the beginning of the operations. Then, the positioning system and the equipment endeavor to follow that straight line to cover the whole field by utilizing operation steering sensor feedback and GNSS data. The systems can also achieve the curved path following which inputs are similar to the straight path.

From the literature review, there are three kinds of positioning systems for an automatic combine harvester; positioning based on machine vision, positioning system based on laser rangefinder, and positioning system based on GNSS. An automatic combine harvester is one

kind of an automatic agricultural vehicle in the used for open field category. The main function of an automatic combine harvester is harvesting.

(1) Positioning system based on machine vision

Around 1980s, when the Personal Computer (PC) became more accessible; which means more compact and reasonable price, a machine vision was utilized for the first time. For agriculture, a machine vision was utilized for the automatic guidance of a vehicle by distinguishing a crop row structure in a field. Benson. E.R. et al. (2003) developed a machine vision-based guidance system for a small-grain harvester. Han. S. et al. (2004) utilized machine vision for vehicle guidance systems. The machine vision is defined as a local sensor because it determines the crop rows only with the relative position of the vehicle. The advantage of machine vision is that its local features have a technological attribute similar to a human operator hence, it has a great potential for utilization of a vehicle positioning system (Wilson, 2000).

The main key to achieve an accurate control of the vehicle for a machine vision-based positioning system is determining position information from a crop row structure. A lot of image processing techniques have been examined to determine the guidance path from crop row images. For example, the development of a binary threshold strategy using a Bayes classification technique to segment crop canopy and soil background for cotton crop effectively and accurately at different growth stages (Reid et al., 1985). The conclusion of Gerrish et al. (1985) proved that threshold intensity images alone will not work in all cases, and the combination of noise filtering, edge detection, threshold and re-scaling was the most potential technique. Marchant and Brivot (1995) utilized Hough transform to find crop rows for the image analysis. Olsen (1995) presented another crop row detection system which does not depend on the segmentation of the crop row by using a low-pass filter to process the pixel's gray value sum-curve to find the offset. Additionally, Hague and Tillet (2001) developed a band-pass filter-based approach to crop row detection and tracking.

(2) Positioning system based on laser rangefinder

The utilization of a laser rangefinder for various application in robotics, i.e., for range measurement and obstacle were discussed (Camrmer and Peterson, 1966). A custom-built laser rangefinder system to continuously monitor a moving vehicle's position were developed (Gordon and Holmes, 1988). The utilization of a laser rangefinder to develop a positioning method using reflectors for infield road navigation was also evaluated. The system was evaluated with differently shaped reflectors to determine the accuracy in positioning (Ahamed et al., 2004). Tsugota et al., (2004) utilized a laser rangefinder for navigation of a small vehicle through an orchard. Subramanian et al., (2006) presented that a guidance system using laser rangefinder is more stable than using GNSS based positioning system in a citrus orchard setting. An automatic navigation system using a Two-Dimensional (2D) laser in an orchard application was developed by using a line detection algorithm based on Hough transform to recognize the three rows which made the vehicle travel through the orchard without collisions (Barawid et al., 2007). Thorpe (1990) from Carnegie Mellon University utilized a Three-Dimensional (3D) scanning laser rangefinder within the framework of NavLab project.

Similar to a machine vison, a laser rangefinder is also defined as a local sensor because it determines the crop rows only with the relative position of the vehicle.

(3) Positioning system based on GNSS

A GNSS refers to a constellation of satellites providing signals from space that transmit positioning and timing data to GNSS receivers. The receivers then use this data to determine location. By definition, GNSS provides global coverage. Example of GNSS include Europe's Galileo, the USA's NAVSTAR Global Positioning System (GPS), Russia's Global'naya Navigatsionnaya Sputnikovaya Sistema (GLONASS), China's BeiDou Navigation Satellite System (European Union Agency for the Space Programme, 2021), India's Indian Region Navigation Satellite System, and Japan's Quasi-Zenith Satellite System (QZSS).

A GPS receiver has been widely utilized as a global guidance sensor since early 1990s (Bell, 2000; Larsen et al., 1994; Yukumoto et al., 2000). For agriculture, many farm works such as tillage, planting, cultivating, and harvesting can be done by utilizing a positioning system based on GPS.

Some agricultural machinery companies and GPS companies, i.e., Trimble Co. Ltd, Topcon Co. Ltd., utilize a GPS and an Inertial Measurement Unit (IMU) to locate the position and orientation of an agricultural vehicle. Then using a computer to calculate the displacement from a navigated path and guides the vehicle to steer automatically.

The positioning system based on GNSS is focusing on making a pre-designed navigation path for an automatic combine harvester by using a GNSS receiver and an Inertial Measurement Unit (IMU) to locate position and orientation of an automatic combine harvester. The advantages of this system are that GNSS can measure absolute coordinate and operation time, which can be reduced while using an efficient pre-designed navigation path. However, the disadvantages of this system are the cost of precise GNSS receiver is very high. In addition, GNSS cannot provide an accurate positioning while using this system under trees or near tall buildings.

1.2 Research objectives

This thesis purpose is to develop a positioning system for an automatic combine harvester. To achieve this purpose, this thesis has three objectives. The first one is to develop a local positioning system based on crop edge detection by integrating a laser rangefinder and machine vision. The second one is to evaluate the performance of QZSS for a combine harvester under static conditions. And the third objective is to examine the feasibility of an auto-guided combine harvester utilizing QZSS as a navigation sensor.

To fulfill the first objective of this thesis, Dempster-Shafer theory was used as a sensor fusion technique to integrate the data from a laser rangefinder and machine vision. To fulfill the second objective of this thesis, the Centimeter Level Augmentation Service (CLAS) and the Multi-Global Navigation Satellite System Advanced Demonstration tool for Orbit and Clock Analysis (MADOCA) positioning augmentation systems which use the signal provided by the QZSS were evaluated in terms of their performance under static conditions. Then to fulfill the third objective of this thesis, both systems were utilized as a navigation sensor for an auto-guided combine harvester to examine the feasibility of utilization.

Results show that the developed crop edge detection system by using sensor fusion has a good certainty of the observation. However, it is not suitable for a practical application. For the performance evaluation of CLAS and MADOCA positioning augmentation systems, the results show that both systems performed good under static conditions. The result of the third objective proved that the CLAS positioning augmentation system is sufficiently good for practical applications while the MADOCA is not suitable for practical applications because it is a time dependent system, the operator has to wait for two to three hours before the operation conditions can be achieved.

1.3 Organization of thesis

This thesis presents a development of positioning systems for an automatic combine harvester. This thesis is organized into six chapters which were listed as follow:
In Chapter 1, the research background; the importance of agricultural automatic vehicles and positioning systems for an automatic combine harvester were introduced. The objective of this thesis was also declared.
Chapter 2 presents the research platform used during the experiments. The test vehicle and the sensors implemented in the experiments are described. Then the conclusion is included.
Chapter 3 describes the development of local positioning systems based on crop edge detection by integrating a laser rangefinder and machine vision. The fundamentals of sensor

fusion theory are described. The results of the simulation were also shown and discussed. Then the whole chapter is concluded.

In Chapter 4, experimental results from the performance evaluation of QZSS under static conditions were discussed. Each parameter in the results is discussed.

In Chapter 5, experimental results from examination of the feasibility of an auto-guided combine harvester utilizing QZSS as a navigation sensor were discussed.

Chapter 6 summarizes the achievements of this study and proposes future work.

CHAPTER 2
RESEARCH PLATFORM

2.1 Introduction

This chapter describes the equipment used during the experiments. The research platform implemented in the Yanmar AG-1100 combine harvester used for the experiments is introduced. Specifications of both the test vehicle and the sensors are included.

2.2 Combine harvester

This study was conducted on a Yanmar AG1100 combine harvester, this combine harvester can work for paddy, wheat, and soybean harvesting. Figure 2.1 shows the original feature of a Yanmar AG1100 combine harvester.

Figure 2.1 Yanmar AG1100 Combine harvester.

2.2.1 Vehicle overview

The combine harvester has 80.9 kW output and the engine rotation speed is 2500 rpm. A 110-liter diesel tank is installed to extend working time. Table 2.1 shows a more detailed specification of the Yanmar AG1100 combine harvester.

Table 2.1 Yanmar AG1100 combine harvester specifications.

Dimension:	
Overall Length:	6,150 mm
Overall Width:	2,350 mm
Overall Height:	2,760 mm
Weight:	4,610 mm
Engine:	
Volume:	3.053 L
Max Output:	80.9 kW
Max Rotation:	2,500 rpm
Fuel Type:	Diesel
Fuel Tank Volume:	110 L
Crawlers:	
Overall Length:	1,780 mm
Overall Width:	500 mm
Distance:	1,185 mm
Transmission:	Full-Time Drive System
Travelling Speed	-2 m/s ~ 2m/s
Header:	
Divider Width:	2,060 mm
Cutter Width:	1,976 mm
Cutting Range (Height):	-100 mm ~ 1,000 mm

Reel Radius × Width:	1,000 mm × 1,915 mm
Rotation Speed:	Synchronized with Crawler
Grain Tank:	
Volume:	1,900 L
Unloading Height:	5,100 mm

Yanmar AG-1100 combine harvester uses the Fulltime Drive System (FDS). Yanmar Co., Ltd., Japan established the FDS with steering wheel by combining the forced differential transmission with the conical steering link in 1998 (Yanmar Co., Ltd., 2020). The combine harvester has an advantage in its movement for straight forward-backward movements by using the FDS with steering wheel. Each crawler of the combine harvester runs at the same speed during the straightforward-backward movements. In addition, Figure 2.3 shows three different ways for turning by utilizing the FDS. The speed of the outside crawler remains the same while the speed of the inside crawler decrease during a gentle turning as shown in Figure 2.3(a). Figure 2.3(b) shows the outside crawler speed remains the same while the inner crawler stops to decrease the turning radius during a normal turn. Then Figure 2.3(c) shows a sharp while the steering angle reaches its maximum level, the inner crawler runs in the opposite direction of the outside crawler (Yanmar Combine harvester, 2020).

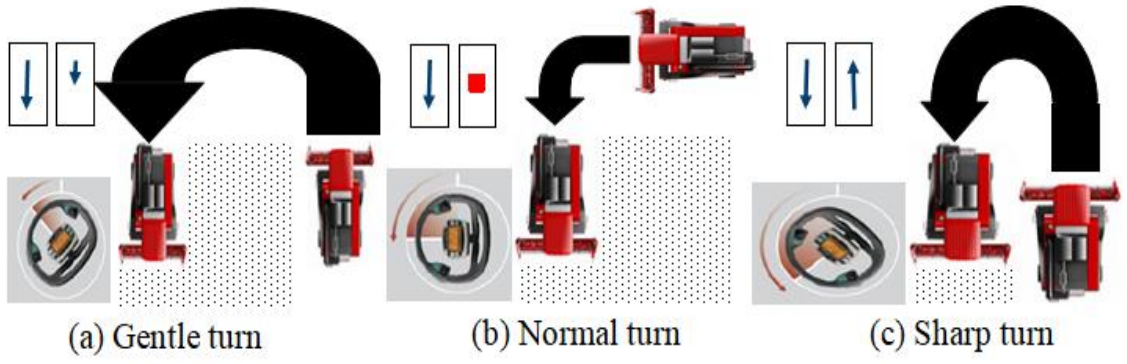

Figure 2.3 Fulltime Drive System (FDS) with steering wheel established by Yanmar Co., Ltd., Japan.

2.3 Local navigation sensors

To determine the navigation information of a vehicle, local navigation sensors aim to measure the position data or local features of the target object in the Region of Interest (ROI) only relative to the position of the vehicle.

2.3.1 RGB camera

Most of RGB cameras are usually equipped with a standard CMOS sensor through which the colored images of persons or objects are captured. A term of Megapixels (MP) is usually used to express the captured static photos. It defines the number of pixels, i.e., length x height, that compose a photo. For the video, MP is usually expressed with interpretative term, i.e., Full HD (1080 x 1920 pixel @ 30 Frame Per Second (fps)) or Ultra HD (3840 x 2160 pixels @ 30/60 fps).

Figure 2.3 The Imaging Source DFK23UM021 RGB camera.

In this study, The Imaging Source DFK23UM021 RGB camera was used to detect crop edge. DFK23UM021 RGB camera is shown in Figure 2.3 and its specification are shown in Table 2.2

Table 2.2 The Imaging Source DFK23UM021 RGB camera specifications.

General Behavior:	
Sensitivity:	0.05 lx
Dynamic range:	8/12 bit
Video formats @ frame rate:	1,280 x 960 (1.2 MP) RGB32 @ 60 fps
(maximum)	1,280 x 960 (1.2 MP) Y800 @ 60 fps
	1,280 x 960 (1.2 MP) Y16 @ 30 fps
	1,024 x 768 (0.8 MP) RGB32 @ 75 fps
	1,024 x 768 (0.8 MP) Y800 @ 75 fps
	1,024 x 768 (0.8 MP) Y16 @ 37 fps
	1,280 x 720 (0.9 MP) RGB32 @ 80 fps
	1,280 x 720 (0.9 MP) Y800 @ 80 fps
	1,280 x 720 (0.9 MP) Y16 @ 40 fps
	640 x 480 (0.3 MP) RGB32 @ 115 fps
	640 x 480 (0.3 MP) Y800 @ 115 fps
	640 x 480 (0.3 MP) Y16 @ 58 fps
Optical:	
Sensor type:	CMOS
Shutter:	Global
Pixel size:	H: 3.75 μm, V: 3.75 μm
Lens mount:	C/CS
Electrical:	
Interface:	USB 3.0
Supply voltage:	4.5 VDC ~ 5.5 VDC
Current consumption:	approx. 250 mA @ 5 VDC
Mechanical:	
Dimensions:	H: 29 mm, W: 29 mm, L: 43 mm
Mass:	65 g

2.3.2 2D laser rangefinder

Figure 2.4 Hokuyo UTM-30LX 2D laser rangefinder.

The Time of Flight (TOF) is a principle that defines a common form of a 2D laser rangefinder operation. It works by sending a laser pulse in a narrow beam towards the object, then measuring the time taken by the pulse to be reflected off the target object and returned to the sensor.

In this study, the Hokuyo UTM-30LX 2D laser rangefinder was used to detect the crop edge. Hokuyo UTM-30LX 2D laser rangefinder is shown in Figure 2.4 and its specification is shown in Table 2.3

Table 2.3 Hokuyo UTM-30LX 2D laser rangefinder specifications.

Power source	
Voltage:	Voltage: 12 VDC ±10%
Current:	Max: 1 A
	Normal: 0.7 A
Light source	Semiconductor laser diode (λ = 905 nm)
	Laser safety Class 1 (FDA)

Detection Range	0.1 m ~ 30 m (White Square Kent Sheet 500 nm or more) Max: 60 m (<30 m guaranteed)
Scan angle	270°
Accuracy	0.1 m ~ 10 m: ±30 mm 10 m ~ 30 m: ±50 mm
Angular resolution	0.25° (360°/1,440 steps)
Scan time	25 ms/scan (40 Hz)
Sound level	<25 dB
Interface	USB 2.0 (full speed)
Synchronous output	NPN open collector
Command system	Exclusively designed command SCIP Ver.2.0
Connection	Power and Synchronous output: 2 m flying lead wire USB: 2 m cable with type-A connector
Ambient	Temperature: -10°C ~ 50°C Humidity: <85% RH (without dew and frost)
Vibration resistance	Double amplitude 1.5 mm 10 Hz ~ 55 Hz, 2 hours each in X, Y and Z direction
Impact resistance	196 m/s^2, 10 times in X, Y and Z direction
Weight	approx. 370 g (with cable attachment)

2.3.3 Pan-Tilt Unit

Pan-Tilt Unit (PTU) allows real-time movement of their payload sensors, increasing the effective field of view of the sensors. For example, by attaching a 2D laser rangefinder to the PTU, it can create 3D information measured by a 2D laser rangefinder.

Figure 2.5 Directed Perception D46 Pan-Tilt Unit.

In this study, the Hokuyo UTM-30LX 2D laser rangefinder was mounted on the Directed Perception D46 Pan-Tilt Unit that moved in the tilt direction to make a sweep scan for the laser rangefinder. Directed Perception D46 Pan-Tilt Unit is show in Figure 2.5 and its specification is shown in Table 2.4

Table 2.4 Directed Perception D46 Pan-Tilt Unit specifications.

Technical specifications	
Rated payload	2.72 kg
Unloaded speed	300°/s Max. @ 30 VDC
Resolution	0.013°
Tilt range	-47° ~ 31°
Pan range	-159° ~ 159°
Input voltage	12 ~ 30 VDC unregulated,
Power consumption	13 W for full power mode @ 30 VDC
Connections & communications	
Host interface	RS-232 (DB-9 female connector)
	RS-422 / RS-485
Control protocols	DP (ASCII, Binary)
Mechanical	Weight: 1.36 kg

	Dimensions: 7.62 cm (H) × 13.03 cm (W) × 10.80 cm (L)

2.3.4 IMU

The Inertia Measurement Unit is used to measure the inclinations of the vehicle which are roll, pitch, and yaw angle. The definition of the roll, pitch, and yaw angle is shown in Figure 2.6. The main reason to measure the inclinations is to determine the vehicle's actual position instead of using the position measured by the GNSS antenna, because the position measured by the GNSS antenna shifts from the Center of Gravity (CG) of vehicles on the ground level. This shift is caused by the inclinations including roll and pitch directions, because the GNSS antenna is always fixed at a higher level over the CG of vehicles.

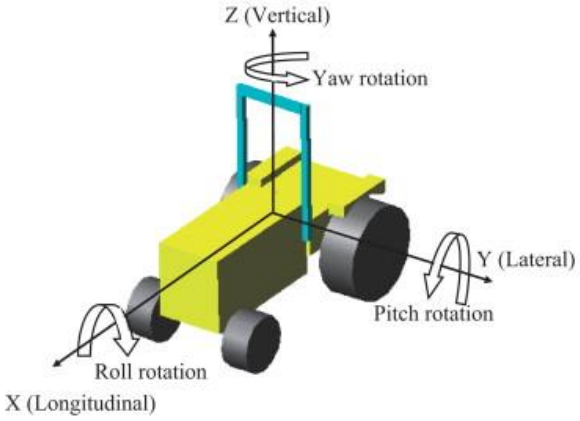

Figure 2.6 Definition of the roll, pitch, and yaw angle.

In this study, VN-100 IMU was used to measure the attitude of the laser rangefinder, angles in roll, pitch, and yaw. Figure 2.6 shows the definition of the roll, pitch, and yaw angle.

Figure 2.7 VN-100 IMU.

The VN-100 IMU is shown in Figure 2.7 and its specification is shown in Table 2.5.

Table 2.5 VN-100 IMU specifications.

Attitude:		
Range:	Roll angle:	±180°
	Pitch angle:	±90°
	Yaw angle:	±180°
Angular Resolution:		< 0.05°
Output Rate:	IMU Data:	800 Hz
	Attitude Data:	400 Hz
Environment		
Operating Temp.:		-40°C ~ -85°C
Storage Temp.:		-40°C ~ -85°C
Electrical		
Input Voltage:		3.2 V ~ 5.5 V
Baud Rate:		Up to 921600
Current draw:		45 mA @ 3.3 V

2.4 Global Navigation Satellite System

A GNSS is a constellation of orbiting satellites providing signals from space that transmit positioning and timing data to GNSS receivers. The GNSS receivers use the data from the

GNSS with an adaptation of trilateration to calculate ground positions. Table 2.6 lists a comparison of the GNSS systems.

Table 2.6 Comparison of GNSS systems.

	Country	**No. of satellites**	**Orbital height**	**Period**
GPS	United States	At least 24 satellites	20,180 km	11.97 hours
GLONASS	Russian Federation	31 (24 operational, 1 in preparation, 2 on maintenance, 3 reserve, 1 on tests)	19,130 km	11.26 hours
Beidou	China	35 satellites in orbit	21,528 km	12.63 hours
Galileo	European Union	22 satellites in orbit; 30 operational satellites budgeted	23,220 km	14.08 hours
IRNASS	India	7 geostationary earth orbit (GEO) satellites	36,000 km	N/A
QZSS	Japan	1 satellite in orbit, 2 satellites in budget	32,618 km	23.96 hours

2.4.1 QZSS

Japan developed a satellite navigation for users around Japan and Oceania called the QZSS. Even in urban canyons and mountainous terrain, the QZSS receiver can still receive the Positioning Navigation and Timing (PNT) broadcast messages. The augmentation signals also can be received by the receiver. These are possible because the space section of the QZSS is an inclined, elliptical geosynchronous orbit of the Quasi-Zenith Navigation Satellites (QZSs). Figure 2.8 shows the shape of Quasi-Zenith Orbit (QZO) which covers the area around Japan and Oceania. To estimate and predict the QZS orbit clock more precisely, the ground section of the QZSS which consists of a Monitoring Station (MS), a Master

Control Station (MCS), Tracking Control Stations (TCS), and the system of other nation research institutes placed around an overseas were utilized.

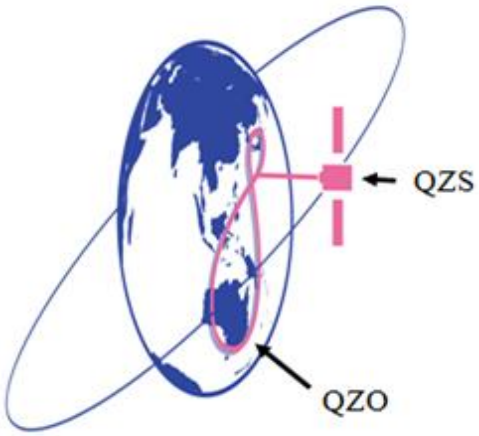

Figure 2.8 The inclined, elliptical geosynchronous orbit shape of QZSs

The GPS interoperable signals are L1C and L1C/A on L1-band (1575.42 MHz), L2C on the L2-band (1227.60 MHz), and L5 on the L5-band (1176.45 MHz). The GPS augmentation signals are L1-Sub-meter class Augmentation with Integrity Function (SAIF) on the L1-band, L6D, L6E on the L6-band (Inaba et al., 2009). The L6D and L6E signals from the QZS are used for the Precise Point Positioning (PPP) service by the CLAS and MADOCA positioning augmentation systems, respectively (Kobayashi, 2020).

The main advantage of the QZSS compared to the Real-Time Kinematic (RTK) positioning augmentation system is that it does not require an Internet Service Provider (ISP) nor an NTRIP service provider to obtain the correction signal from the reference station.

2.4.2 Magellan GNSS receiver

Magellan MJ-30080-GM-QZS receiver and its own antenna are shown in Figure 2.9. This receiver and antenna were used in this research to provide CLAS and MADOCA positioning

augmentation systems. Table 2.7 and Table 2.8 show specifications of Magellan MJ-30080-GM-QZS receiver and its own antenna, respectively.

Figure 2.9 Magellan MJ-30080-GM-QZS receiver and antenna.

Table 2.7 Magellan MJ-30080-GM-QZS receiver specifications.

Module Utilization	Multi frequency GNSSRTK / PPP Module
GNSS System: Signal	GPS: L1, L2, L5 QZSS: L1, L2, L5, L6 GLONASS: G1, G2 Galileo: E1, E5a, E5b, E5 Beidou: B1, B2
Initial position calculation time	Cold start: 90 s Warm start: 35 s Hot start: 12 s Satellite reacquisition time: 4s
Position accuracy (RMSE)	Autonomous positioning: 1.5 m RTK – dynamic: 5 cm + 0.7 ppm x baseline length (< 30 km) RTK – static: 0.5 cm + 0.7 ppm x baseline length (< 30 km)

	PPP (MADOCA): < 10 cm PPP-RTK (CLAS) – dynamic: < 6.94 cm PPP-RTK (CLAS) – static: < 3.47 cm
Maximum output rate	100 Hz
Input / Output interface	RS232C x 2 Ethernet x 1 (Optional)
Data format	NMEA0183 version 3.0 (Output) RTCM SC104 version 3.2 (Input / Output
Dimensions	206.2 (W) x 155 (D) x 86 (H) mm
Weight	1500 g
Power consumption	Below 10 W
Power supply	DC 12 V

Table 2.8 Magellan MJ-30080-GM-QZS antenna specifications.

GNSS system : Signal	GPS: L1, L2, L5 QZSS: L1, L2, L5, L6 GLONASS: G1, G2 Galileo: E1, E5a, E5b, E5, E6 Beidou: B1, B2, B3 SBAS: L1
Dimensions	148 (Φ) x 60 (H) mm (Excluding base)
Weight	405 g (Excluding base)
Operating Voltage range	3.3 ~ 15.0 V
Current consumption	Below 40 mA

2.4.2.1 CLAS

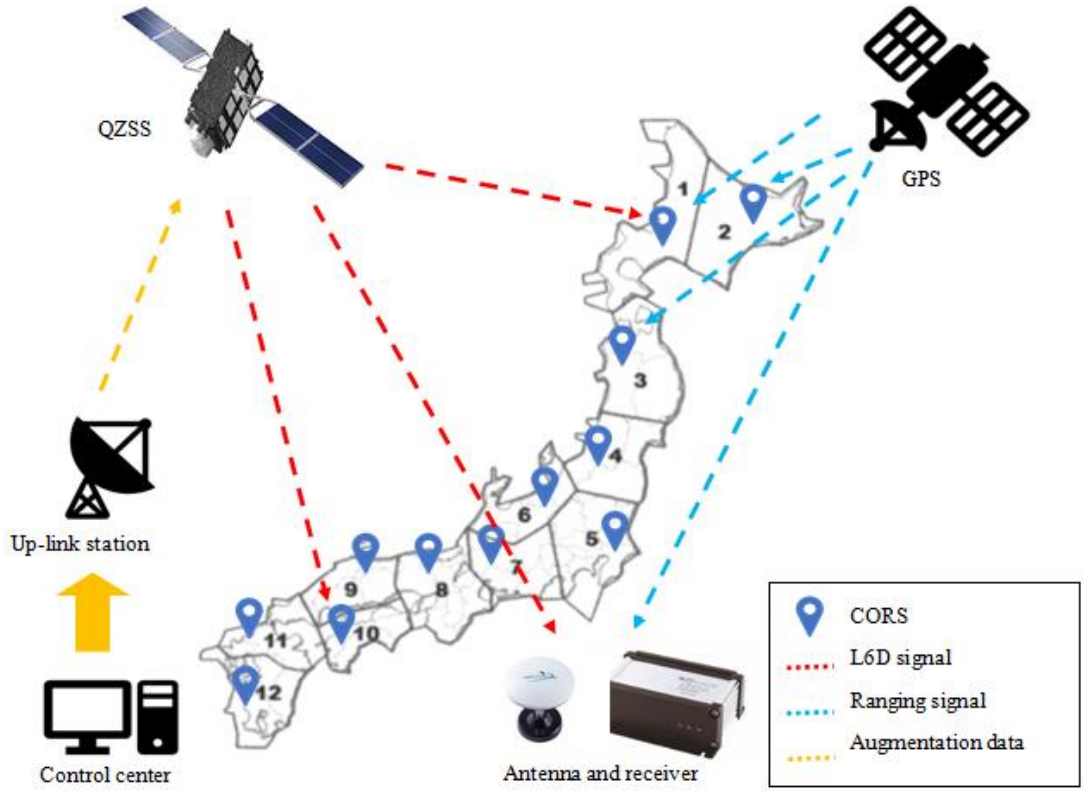

Figure 2.10 Diagram of the CLAS positioning augmentation system.

The Centimeter-Class Augmentation System (CMAS) is a prototype for the development of the CLAS by omitting a complementary function for GPS. The diagram of the CLAS is shown in Figure 2.10. The QZS broadcast the augmentation information via the L-band Experiment (LEX) signal (Saito et al., 2011) which was renamed to L6 in the latest QZSS revision; the red-dash line in Figure 2.10 displays the L6D signal. To estimate distance-dependent GNSS errors, the CMAS uses the State Space Modeling and the wide-area dynamic error model from the GPS and the QZS data monitored by the GEONET (Wübbena et al., 2005). The CMAS generates the correction information in the State Space Representation (SSR) form via the LEX signal which applied to PPP-RTK (Saito et al., 2011; Seigo et al., 2015). The correction of the positioning error consists of satellite orbit

corrections, satellite clock correction, satellite phase biases, and ionosphere and troposphere delays. However, the CMAS generates the correction of the ionosphere and troposphere delays for an area of the QZSS's coverage similar to the Virtual Reference Station- RTK (VRS-RTK) system. Therefore, there is a limitation for using the CMAS all over the country simultaneously (Wang and Noguchi, 2019). Due to the succession of the CMAS, the CLAS distributes the service arena with an addition of artificial grid points covering each area with an interval of 60 km which are used for the ionospheric and tropospheric delay correction. The distribution of these twelve parts of GEONET called the Continuously Operation Reference Stations (CORS) are displayed by the blue pinpoints in Figure 2.10. The user corrects its own observations and gives centimeter-accuracy solutions within 1 minute using the PPP-RTK positioning method (Miya et al., 2016). The L6D signal which contains the satellite orbit and the satellite clock corrections, ionospheric and troposphere delays from the QZS to the user is obtained by the CLAS receiver. Please keep in mind that the LEX band was changed to L6-band which has 2 channels; L6D for the CLAS and L6E for the MADOCA.

To make a comparison or to use the positioning result of VRS-RTK and PPP-RTK together requires the coordinate transformations for compensation because the CLAS neglects the crustal movement of the earth (Wang and Noguchi, 2019).

2.4.2.2 MADOCA

The Japan Aerospace Exploration Agency (JAXA) developed the MADOCA positioning augmentation system. Figure 2.11 shows the diagram of the MADOCA positioning augmentation system. By using the technology from JAXA, the MADOCA can estimate the satellite orbit and clock correction. And it supports all usable GNSS systems; GPS, GLONASS, Galileo, etc. The red-dash line in Figure 2.11 displays the L6E which broadcast the correction of the positioning error including satellite orbit corrections and satellite clock from the QZSS. However, the ionosphere and troposphere delays cannot be estimated by the

MADOCA because the global monitoring station of the MADOCA (MGM-net) displayed by the red-pinpoint in Figure 2.11 is not dense comparing to the CORS of the CLAS displayed by blue-pinpoint in Figure 2.10. On the other hand, these delays could be estimated by the MADOCA receiver (Zhang et al., 2019). The drawback of the MADOCA is that it requires a long time to recover to a convergent PPP positioning method (Kobayashi, 2020).

Similar to the CLAS, to make a comparison or to use the positioning results of VRS-RTK and PPP-RTK together requires the coordinate transformations for compensation because the MADOCA also neglects the earth's crustal movement.

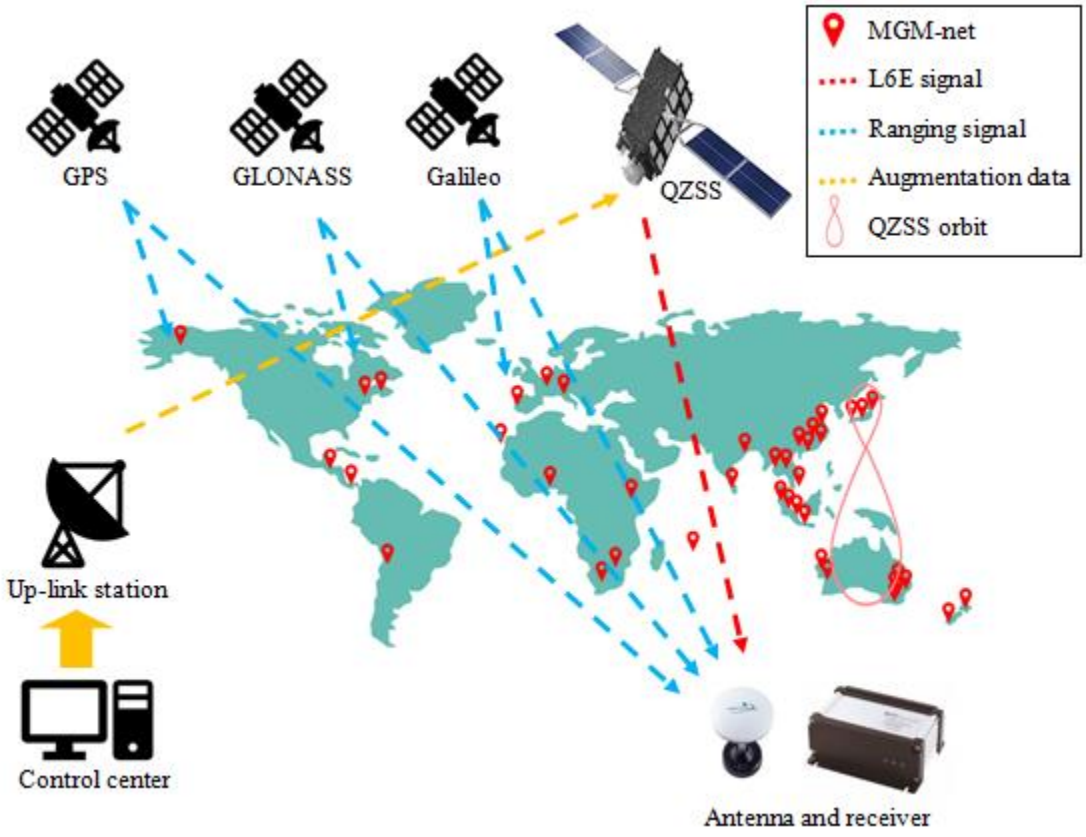

Figure 2.11 Diagram of the MADOCA positioning augmentation system.

2.4.3 Trimble GNSS receiver

Trimble SPS855 receiver and its own antenna are shown in Figure 2.12. This receiver and antenna were used in this research to provide RTK positioning augmentation system. The specification of Trimble SPS855 receiver and its own antenna are shown in Appendix A. The purpose of using RTK positioning technique is to use it as a reference position for the performance evaluation of the CLAS and MADOCA.

Figure 2.12 Trimble SPS855 receiver and antenna.

2.4.3.1 RTK-GPS

The basic principle of the RTK-GPS is described as follows. Two small-area wireless communication GNSS receivers were connected via RS232C to the reference receiver as a base station and the rover receiver for the correction of the RTK signal communication. The rover receiver receives the measurement of the satellites and location of the reference receiver. Then, the rover receiver calculates its location relative to the reference receiver. The drawback of the RTK position technique is the reference receiver is the correction data could be blocked by the high building or trees, which limited the rover receiver into a certain area.

However, this research used a VRS from an ISP, mainly because the purpose of utilize the RTK positioning technique is to enhance the precision of the positioning data from the GNSS

to a centimeter-level in real-time. By using the VRS the RTK correction signal can be received via an ISP. The Multiple Reference Station (MRS) is an original concept of the VRS because VRS uses the surrounding area of interest's MRS network, but it does not require an actual physical reference station close to the user. The VRS can achieve single-point coordinate accuracies of 2 cm with reference stations separated by 50-70 km under ideal conditions (Castleden et al., 2004).

2.4.4 GNSS splitter

The GNSS splitter used in this research is the GPS Networking Amplified Loaded DC Blocked Splitter 1X2 (ALDCBS1X2) GNSS splitter. It is a one input, two outputs amplified GNSS splitter based on the Wilkinson splitter design. The frequency response covers the entire L-band (all GNSS frequencies) with excellent gain flatness. The purpose of using the GNSS splitter in this research is to divide the GNSS signal from a single antenna into two GNSS receivers meaning both receivers can receive the GNSS signal at the exact same position of the antenna. However, the measured position from both receivers might be different due to the different characteristic of GNSS system. Figure 2.13 shows the ALDCBS1X2 GNSS splitter. In addition, the datasheet of this GNSS splitter can be found in Appendix B.

Figure 2.13 GPS Networking ALDCBS1X2 GNSS splitter.

2.5 Conclusion

This chapter described the equipment used in this research. The research platform used for each evaluation and test was explained section by section. The technical specifications of the vehicle, sensors, and equipment were introduced. The purpose of the explanation of each sensor is highlighting their most relevant aspects for the experiments.

CHAPTER 3
LOCAL POSITIONING SYSTEM BASED ON CROP EDGE DETECTION BY INTERGRATING A LASER RANGEFINDER AND MACHINE VISION

3.1 Introduction

A rapidly emerging discipline of intelligent sensor processing in scientific and engineering research can assist researchers in the systems development, which can achieve environment visibility and comprehension by using new computational methods and tools. Dynamic sensors data in multiple dimensions and interaction between individual sensors are regarded as applications of sensor processing to image and signal processing. The measurement of sensors in scalar values or vector values is most often a function of time and space.

Multi-sensor fusion has received the attention of researchers. Publishing of articles with new methods and theories ordinary appeared in journals specializing in a large range of subjects, including aerospace engineering, robotics, statistics, and artificial intelligence.

Sensor fusion is the process of combining features observed by multiple sensors into a coherent form (Murphy, Arkin, 1992). It makes a system less susceptible to the failure of a single component. A system gets more accurate information by combining measurement from several different kinds of sensors. In addition, a system is less sensitive to noise and temporary glitches by combining measurements from the same sensor.

This chapter presents the fundamental of sensor fusion and its theory. Then, the experiments methodology is described. The results from each sensor and sensor fusion are presented and discussed.

3.1.1 Sensor's uncertainty and accuracy

Sensor have varying accuracy. They rarely provide absolute value for a physical variable. Even though a sensor could provide absolute value, the measured physical values are usually vary over time. A value range in order to accurately represent the environment would be returned from the sensor measurement that covers a finite time period.

The concept of limited accuracy is as factor in all data processing. Generally, all data representation has upper and lower boundary for a maximum number of digits of accuracy and the representable values. The important information can be lost, or the result of calculations can be disastrously in error if limits in accuracy are not manipulated appropriately.

The primary problem is how to manipulate with uncertainty in sensor data. Fusing sensor measurement would be a simple and straightforward operation if sensor data were reliable and accurate. In many cases, the reliable measurement recognition is significant as the recognition of exact values returned by a sensor. To manipulate sensor uncertainty, three theories are proposed and described in the next section.

3.1.2 Theory of sensor fusion

(1) Bayesian probability theory

Bayesian probability theory provides a mathematical framework by using probability to perform inference or reasoning. Around 200 years ago, the basis of this theory was established by many scientists such as Bernoulli, Bayes, and Laplace, but modern statisticians have held suspect or controversial about this theory. However, by the occurrence of a "Bayesian revolution" during the last few decades, Bayesian probability theory is now ordinarily applied in many scientific disciplines, from astrophysics to neuroscience. The

relative validity of hypotheses in the face of noisy, sparse, or uncertain data, or to adjust the parameter of a specific model can be judged by using this theory

Bayesian probability theory has a rule called Bayes' rule. This rule indeed involves only the manipulation of conditional probabilities. The joint probability of two events, A and B, can be expressed as equation (3.1) and (3.2)

$$P(AB) = P(A|B)P(B) \quad (3.1)$$

$$= P(B|A)P(A) \quad (3.2)$$

In Bayesian probability theory, the relative truth of the hypothesis (H) given the data (D) according to Bayes' rule relation, is shown by equation (3.3)

$$P(H|D) = \frac{P(D|H)P(H)}{P(D)} \quad (3.3)$$

The term $P(H|D)$ is called the likelihood function. The probability of the observed data occurring from the hypothesis is estimated by the likelihood function. The term $P(H)$ is called the prior. It reflects prior knowledge before the data consideration. For the Bayesian probability theory, the specification of the prior is often the most subjective criterion. The reason statisticians held Bayesian inference in contempt because of the specification of the prior. However, making up one's assumption and directly exposing of an element of subjectivity in the reasoning process are the advantages of Bayesian probability theory. The term $P(D)$ is an ignorable normalizing constant, and it is obtained by summing $P(D|H)P(H)$ overall H. The term $P(H|D)$ is the posterior. It analyzes the probability of the hypothesis after the data are considered.

Similar to equation (3.3) the probability of H given a set of observations $D_1, D_2, \dots, D_n$ can be expressed by equation (3.4)

$$P(H|D_1, \dots D_n) = \frac{\frac{P(H)}{P(\neg H)} \prod_{i=1}^{n} \frac{P(D_i|H)}{P(D_i|\neg H)}}{1+\frac{P(H)}{P(\neg H)} \prod_{i=1}^{n} \frac{P(D_i|H)}{P(D_i|\neg H)}} \quad (3.4)$$

Bayesian probability theory for sensor fusion has certain drawbacks. The requirement of knowledge of the prior probability distribution $P(D_i|H)$ and $P(D_i)$, which may not always be available is an immediate problem. And the subjective judgements are often important when defining the prior probabilities. This theory requires that all information be at the same level of abstraction. Another problem is the unstable of probabilities found by this theory when the number of unknown propositions is larger than the number of known propositions.

(2) Dempster-Shafer theory

Dempster-Shafer theory arose from the reinterpretation and development by Arthur Dempster and Glenn Shafer to make the method of reasoning with uncertain information, with understood connections to other frameworks such as probability, possibility, and imprecise probability theories. The Dempster-Shafer theory is regarded as a generalization of the Bayesian probability theory. The main difference between these two theories is that the prior probability distribution is not the requirement of the Dempster-Shafer theory.

In Dempster-Shafer theory, the establishing of a set that contain the null set ($\emptyset$), and every single hypothesis (singleton) considered; this set was regarded as a frame of discernment (Θ), is the primary step of the theory. Generally, probability theory works on every element of Θ, but DS theory examine every of the power set of Θ (2^{Θ}).

If each element of 2^{Θ} is considered a proposition A_i means each sensor observation assigns probability values to at least one, and possibly a very large number, of the A_i. The relationship of 2^{Θ} and A_i can be described by equation (3.5).

$$\sum_{A_i \in \Theta} m(A_i) = 1 \quad (3.5)$$

$$\text{If;} \quad \Theta = \{a, b\}$$

$$2^{\Theta} = \{\emptyset, \{a\}, \{b\}, \Theta\}$$

$$m(\emptyset) = 0$$

Where; $m(A_i)$ is the probability mass of a proposition A_i

$m(\emptyset)$ is the probability mass of null set ($\emptyset$)

The equation (3.5) requires that any probability not attributed to a proper subset of Θ is then given to Θ. Therefore, the value $m(\Theta)$ is a measure of the uncertainty in the system.

The use of probability mass functions defines the two principal components of the Dempster-Shafer theory.

1) Belief or support function is the minimum probability for hypothesis A.
2) Plausibility function is the maximum probability for hypothesis A.

The relationship between both components can be described by the following equations.

$$Bel(A) = \sum_{A_i \subseteq A} m(A_i) \quad (3.6)$$

$$Pl(A) = 1 - \sum_{A_i \cap A \neq \emptyset} m(A_i) \quad (3.7)$$

$$= 1 - Bel(\neg A) \quad (3.8)$$

Therefore, $[Bel(A), Pl(A)]$ is the uncertainty function of A. In the Bayesian probability theory, the value of uncertainty function is forced to be 0.

To combine any two-belief function; A and B over the same Θ with at least one focal element in common into a new belief function, Dempster-Shafer theory has Dempster's rule of combination to perform which is shown in the following equations.

$$m(C_k) = m(A_i) \oplus m(B_j) \quad (3.9)$$

$$m(C_k) = \frac{\sum_{A_i \cap B_j = C_k, C_k \neq \emptyset} m(A_i) m(B_j)}{\sum_{A_i \cap B_j \neq \emptyset} m(A_i) m(B_j)} \quad (3.10)$$

From equation (3.10), the denominator is distribution of any mass associated with $\emptyset$ intersections of belief to the nonempty intersections. The output to a belief function is renormalized by this denominator. Counterintuitive results may occur when renormalize in extreme cases. For example, in the case that show a feature must be either a, b, or c. Sensor$_1$ is combined with contradictory evidence for sensor$_2$. The belief function of each sensor is shown below.

$$Bel_1(A) = [m(\{a\}) = 0.80, m(\{c\}) = 0.20]$$
$$Bel_2(A) = [m(\{b\}) = 0.80, m(\{c\}) = 0.20]$$

From the above belief function, $Bel_1(A)$ and $Bel_2(A)$ eliminate a and b by canceling each other, leaving the result is total support for c. However, it seems to be unreasonable. Therefore, the weight of conflict metric was established and will be described in the next paragraph.

In order to deal with the combination of contradictory evidence problem, the weight of conflict metric (Con) was established by Shafer. And it can be estimated by using an equation (3.11).

$$Con(Belief_1, Belief_2) = \log\left(\frac{1}{1-\kappa}\right) \quad (3.11)$$

Where; $\kappa = \sum_{A_i \cap B_i = \emptyset} m(A_i) m(B_j)$

$Con = [0, \infty]$

if; $\kappa \to 0.0$, $Con \to 0.0$

$\kappa \to 1.0$, $Con \to \infty$

(3) Fuzzy logic

Fuzzy logic uses fuzzy sets to deal with sensor fusion problems. It is a type of multivalued logic. Fuzzy sets and fuzzy logic can be proposed as a general theory that attaches probability and Dempster-Shafer theory as special cases. Fuzzy sets are similar to traditional set theory unless that fuzzy set's member has a participatory value authorized by a membership function that quantifies the number of memberships the element has in the function.

In addition to membership, fuzzy sets contain a number of functions that are similar as the function operated on traditional sets. Generally, the operations of complementation, union, and interaction with fuzzy sets contain a number of possible functions. Similarly, to deal with the uncertainty, fuzzy logic proposes a simple framework. However, representation of the suitable number of possible implementations of fuzzy sets and fuzzy logic is cumbersome.

Measurement theory and the development of fuzzy controllers are two areas that are nearly associated to the sensor fusion problems and possible a number of existing methods could be described in terms of fuzzy methodology. A pattern recognition and inference of statistical parameters are also related areas with the fuzzy techniques. These mentioned areas show the potential of fuzzy methodology dealing with the sensor fusion problems. The other exceptional interest areas which are associated to fuzzy methodology are articular neural networks, and genetic algorithms.

From the study of the three theories of sensor fusion introduced in this chapter, Dempster-Shafer theory was selected as sensor fusion method to develop the local positioning system based on crop edge detection by integrating a laser rangefinder and machine vision. Dempster-Shafer theory does not require the prior probability distribution which is suitable for the real-time positioning. In the real-time positioning, there is unknown prior probability distribution. In contrast, Bayesian probability theory requires the prior probability; therefore, it is not suitable for the real-time positioning. For the fuzzy logic, the efficiency of the system depends on the internal system design. Thus, it is not suitable for this academic research.

3.2 Materials and methods

The simulation experiments by using the card boxes were conducted to test the observation certainty of the developed system. The purpose of using the card boxes is to simulate them as the crops. The overall experiment is shown in Figure 3.1 and Figure 3.2.

Figure 3.1 Simulation experiment to detect the edge of box.

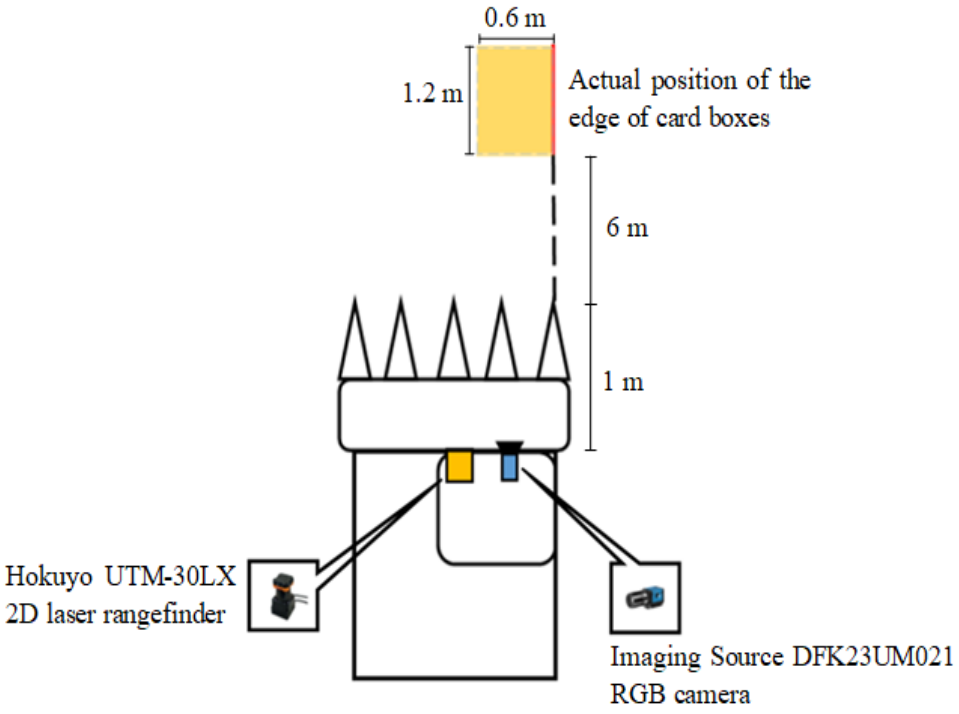

Figure 3.2 Diagram of simulation experiment.

The actual position of the edge of card boxes was collected by measurement. Figure 3.2 shows a diagram of the simulation experiment; the actual position of the edge of card boxes, the position of the RGB camera and the laser rangefinder on the combine harvester.

In fact, the system also detects the edge of card boxes on the left side. However, this study focused only the edge of card boxes on the right side because a combine harvest usually runs along the left side of cut area during the harvesting. Therefore, in this local positioning system based on crop edge detection, the combine harvester runs along a guidance path by the end of the header on the right side which moves along the detected edge.

The simulation experiment was conducted in three parts; the RGB camera detects the edge of the card boxes, the laser rangefinder detects the edge of the card boxes, and the sensor fusion detects the edge of the card boxes.

(1) RGB camera detects the edge of the card boxes

Figure 3.3 Input image from RGB camera.

Figure 3.3 shows the input image acquired from the RGB camera. After acquiring the input image, the ROI was marked off on the input image as shown in Figure 3.4

Figure 3.4 Input image with ROI.

The Inverse Perspective Mapping (IPM) was applied to remove the perspective effect. IPM is a technique that geometrically transforms an image by constructing a new on inverse 2D planar by projecting each of the pixels of a 3D object in a 2D perspective view and remapping them to new positions. IPM uses intrinsic parameters of the camera; angular view, aperture, and resolution; and extrinsic parameters of the camera; pitch angle, yaw angle, and height above ground to remove the perspective effect.

Equation (3.12) is used defined the mapping function from Image Space (Space I) to Surface space (Space S).

$$(u, v) = h_c * \cot[(\bar{\theta} - \alpha) + u\frac{2\alpha}{n-1}] * \cos[(\bar{\gamma} - \alpha) + v\frac{2\alpha}{m-1}] + l \quad (3.12)$$

$$y(u, v) = h_c * \cot[(\bar{\theta} - \alpha) + u\frac{2\alpha}{n-1}] * \sin[(\bar{\gamma} - \alpha) + v\frac{2\alpha}{m-1}] + d$$

$$z(u, v)] = 0$$

Where; $\bar{\gamma}$ is yaw angle of the RGB camera

θ is pitch angle of the RGB camera

h_c is the height of the camera from the ground

l is the longitudinal of the RGB camera to the center of origin on the xy plane

d is the transverse distance of the RGB camera to the center of origin on the xy plane

2α is the angular aperture

$m * n$ is the image resolution

To remove the perspective effect, equation (3.13) defines the projection transformation, which recovers the texture of the Space S.

$$u(x, y, 0) = \frac{\arctan\left\{\frac{h\sin\left[\arctan\left(\frac{y-d}{x-l}\right)\right]}{y-d}\right\} - (\bar{\theta} - \alpha)}{\frac{2\alpha}{n-1}} \quad (3.13)$$

$$v(x, y, 0) = \frac{\arctan\left[\frac{y-d}{x-l}\right] - (\bar{\gamma} - \alpha)}{\frac{2\alpha}{m-1}}$$

After applying equation (3.12) and (3.13), the window of interest from the input image can be projected onto the ground plane. Figure 3.5 shows image transformed by the IPM

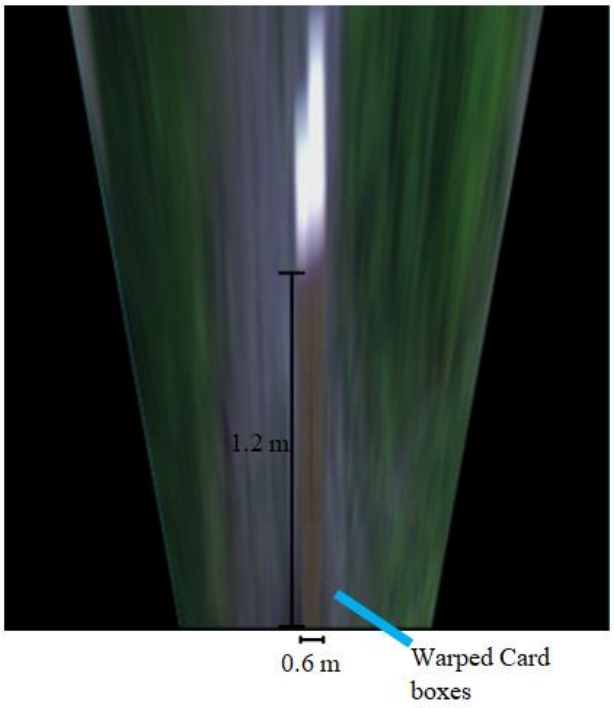

Figure 3.5 IPM image.

The IPM images, transformed in the RGB color space have a changing of radical brightness in the surroundings due to shadows, dust particles floating in air, and any potential noise. Therefore, a robust segmentation method is necessary to filter out the noise in the image and extract the box.

To distinguish crops from other image elements, color indices have been developed (Woebbecke, et al., 1995). By the image transformation into these indices, the spectral difference between plants and the rest of the image area are contrasted.

In this study, the excess blue minus excess red index (ExBR), based on the visible spectral indices proposed by early researchers, has been applied to the image to perform segmentations. ExBR can be estimated by equation (3.14)

$$r = \frac{R}{R+G+B}, g = \frac{G}{R+G+B}, b = \frac{B}{R+G+B} \quad (3.14)$$

Excess blue: ExB = $1.4b - g$

Excess red: ExR = $1.4r - g$

Excess blue minus excess red: ExBR = ExB – ExR

Where R, G, and B are normalized RGB coordinates that range from 0 to 1 and can be estimated from equation (3.15)

$$R = \frac{R}{R_{max}}, G = \frac{G}{G_{max}}, B = \frac{B}{B_{max}} \quad (3.15)$$

Where $R_{max} = G_{max} = B_{max} = 255$. Therefore, on the basis of normalized RGB coordinates, these indices become insensitive to the changes that arise from ambient light conditions as well as the differences in the angles to target surfaces. Figure 3.6 shows the result of the box segmentation by applying the ExBR method to transform IPM image.

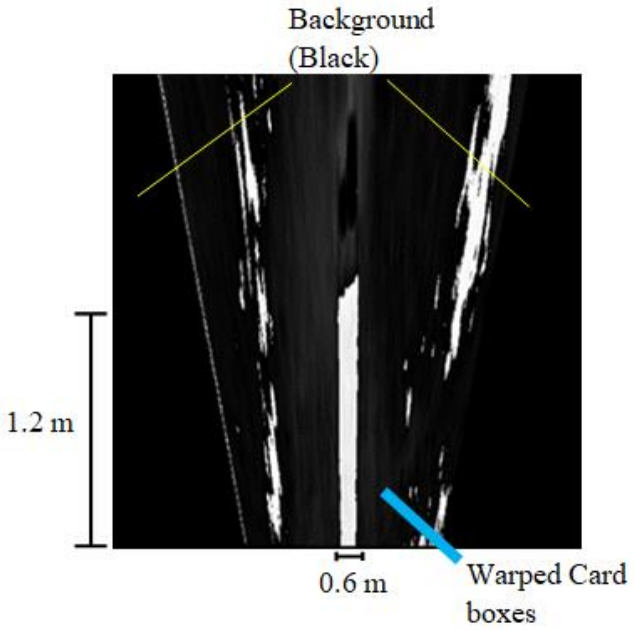

Figure 3.6 Applied ExBR method to IPM image.

The edge of card boxes on the right side was detected by the outer-most boundary point of the boxes area from the image. The detected edge of card boxes represented by red line is shown in Figure 3.7

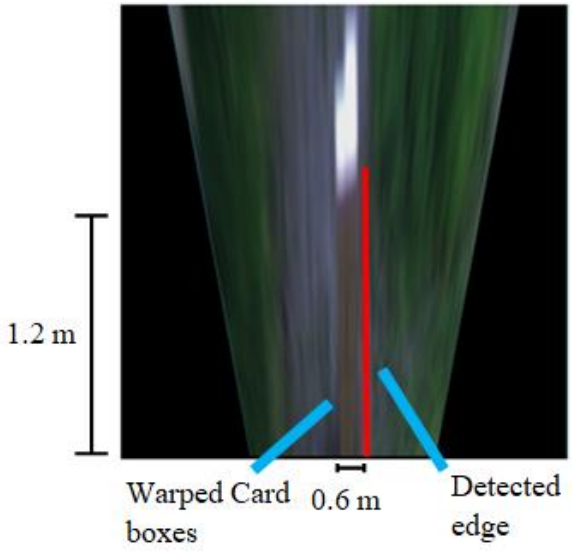

Figure 3.7 The detected edge of card boxes by RGB camera.

(2) Laser rangefinder detects the edge of the card boxes

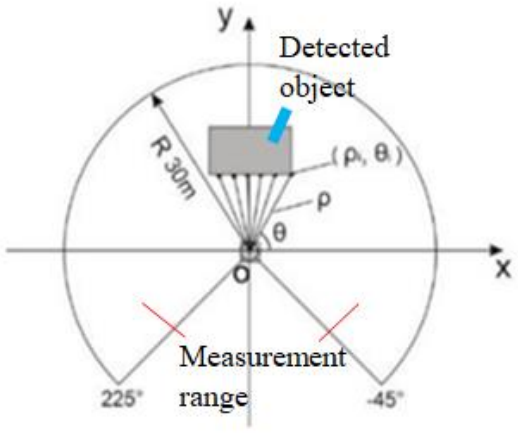

Figure 3.8 Schematic diagram of laser rangefinder.

Figure 3.8 shows the schematic diagram of the laser rangefinder. The laser rangefinder reference system is $R = (x_L, y_L)$. The origin O is in the center of the half-circle scanning range of the laser rangefinder. The laser beam operates a counterclockwise sweeping from -45° to 225°. Therefore, the laser rangefinder gives the position of each detected point in polar coordinates (ρ, θ). Equation (3.16) shows the data logged by the laser rangefinder in a 2D coordinate system.

$$\begin{bmatrix} x_L \\ y_L \\ z_L \end{bmatrix} = \begin{bmatrix} \rho * \cos(\theta_L) \\ \rho * \sin(\theta_L) \\ 0 \end{bmatrix} \tag{3.16}$$

Where; ρ is distance between the reference origin and the object's detected point.

θ_L is angle between the x_L axis and the beam direction.

Equation (3.17) describes the coordinate transformation from the laser rangefinder's coordinates system $(x_{L,}y_L)$ into the vehicle's Cartesian coordinate system (x, y, z) by considering the rotation on the pitch direction and the inclination on the roll direction.

$$\begin{bmatrix} x \\ y \\ z \end{bmatrix} = \begin{bmatrix} \cos(\theta_r) & 0 & \sin(\theta_r) \\ -\sin(\theta_r)\, sin\,(\theta_p) & \cos(\theta_p) & \cos(\theta_r)\sin(\theta_p) \\ -\sin(\theta_r)\, cos\,(\theta_p) & -sin\,(\theta_p) & \cos(\theta_r)\cos(\theta_p) \end{bmatrix} \begin{bmatrix} x_L \\ y_L \\ z_L \end{bmatrix} + \begin{bmatrix} 0 \\ 0 \\ H \end{bmatrix} \tag{3.17}$$

Where; θ_r is angle on roll direction collected by IMU.

θ_p is angle in pitch direction collected by IMU.

H is height of the laser rangefinder.

The data set from the laser rangefinder contain two classes of measurements; the card boxes measurement and the ground measurement. The optimum threshold between the two classes of measurements can be estimated by Otsu's method, and it is shown by equation (3.18). Then the edge of card boxes on the right ride was detected by using the least square method.

$$\sigma_w^2 = \sum_{i=0}^{u}(u_i - \mu_1)^2 * \frac{u^*}{u_{max}} + \sum_{i=u^*+1}^{u_{max}}(u_i - \mu_2)^2 * \frac{u_{max} - u^*}{u_{max}} \tag{3.18}$$

$$\sigma_B^2 = \frac{u^*(\mu_1 - \mu)^2 + (u_{max} - u^*)(\mu_2 - \mu)^2}{u_{max}}$$

$$maximize(\frac{\sigma_B^2}{\sigma_w^2}) \rightarrow u_{opt}$$

Where; σ_w^2 is intra-class variance.

σ_B^2 is between-class variance.

u^* is the separation of two classes.

μ is mean of the two classes.

μ_1 is mean of class 1.

μ_2 is mean of class 2.

u_{opt} is optimum demarcation of two classes.

(3) Sensor fusion detects the edge of the card boxes

In this study, Dempster-Shafer theory is used for sensor fusion in the Sensor Fusion Effect (SFX) architecture. The functional layout of the SFX architecture is shown in Figure 3.9. SFX is a reusable generic control scheme for intelligent sensor fusion. Sensor fusion in SFX contains three distinct activities;

1) Configuration is the activity which burden with using the task goals of a robot to create expectations of percept and to anticipate which features of the percept will be observable to which sensor and the consequence of their contribution.
2) Uncertainty management is the activity which gather observations and calculates the total belief in the percept using a Dempster-Shafer framework. It consists of three steps; the first step is the collecting step which collects the features observations from each sensor. The second step is the preprocessing step which extracts features from the observation and fusion at the feature level. During this step, missing or abnormal observations trigger exception handling activity. And the third step is the fusion step, which transfers belief to common Θ, combines the resultant belief functions, and determine the conflict between beliefs.

3) Exception handling is the activity which receives missing or abnormal observations of each sensor. Then, diagnose the problem and recovery.

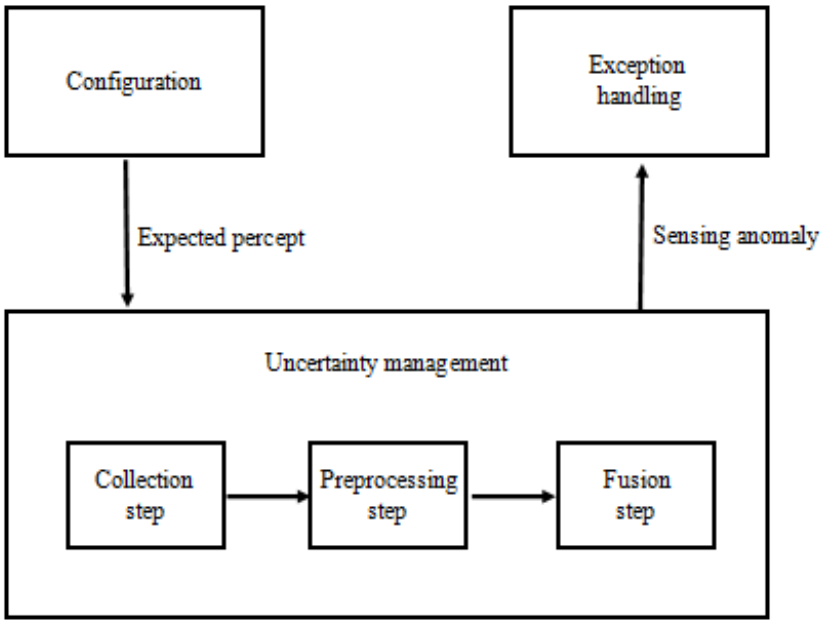

Figure 3.9 Functional layout of the SFX architecture.

The accumulated evidence in SFX follows a three-level hierarchy; evidence for a feature, evidence for a description of percept, and evidence for an observation of the entire percept. Each evidence is substitute as a Dempster-Shafer belief function. The explanation of each evidence is described below.

1) Evidence for a feature ($\varepsilon_{d_j^i}^{s^k}$) is based on how well the expected value matches the observed value of the feature. Considering the uncertainty and variation arising from the particular sensors and feature-extraction algorithms used in the observation. It can be done by using descriptions constructed from example sensor data. The belief function for a feature is indicated by $Bel_{d_j^i}^{s^k}|2^{\Omega}: m(d_j^i), m(\bar{d}_j^i), m(\Omega)$.

2) Evidence for a description of percept ($\varepsilon_{d^i}^{s^k}$) is leaded by the evidence from each feature in a particular description of a percept. The belief function for a description is indicated by $Bel_{d^i}^{s^k}|2^{\Phi}: m(d^i), m(\bar{d}^{\iota}), m(\Phi)$. The transformation from the belief function for a feature to the belief function for a description can be done as shown in the equation (3.19).

$$r_{d^i}: Bel_{d_j^i}^{s^k} \Big| 2^{\Omega} \rightarrow Bel_{d^i}^{s^k} \Big| 2^{\Phi} \tag{3.19}$$

$$m(d^i) = r_{d_j^i}\, m(d_j^i)$$

$$m(\bar{d}^{\iota}) = r_{d_j^i}\, m(\bar{d}_j^i)$$

$$m(\Phi) = 1 - m(d^i) - m(\bar{d}^{\iota})$$

Where; $r_{d_j^i}$ = description interpretation enlargement function.

3) Evidence for an observation of the entire percept (ε_p); each body of evidence for the description in the expected percept is used to generate the total measure of evidence. The belief function for a percept is indicated by $Bel_p^{d^i s^k}|2^{\Theta}: m(p), m(\bar{p}), m(\Theta)$. The transformation from the belief function for a description to the belief function for a percept can be done as shown in equation (3.20)

$$r_p: Bel_{d^i}^{s^k}|2^{\Phi} \rightarrow Bel_p^{d^i s^k}|2^{\Theta} \tag{3.20}$$

$$m(p^i) = r_p\ m(d^i)$$

$$m(\bar{p}^{\iota}) = r_p\, m(\bar{d}^{\iota})$$

$$m(\Theta) = 1 - m(p^i) - m(\bar{p}^{\iota})$$

Where; r_p = percept interpretation enlargement function

After obtaining the belief function for a percept of each sensor, it is possible to use the Dempster's rule of combination as shown in equation (3.10) to combine those two belief functions.

3.3 Results and discussion

According to the previous section, the results are divided into three parts; the RGB camera detects the edge of the card boxes, Laser rangefinder detects the edge of the card boxes, and sensor fusion detects the edge of the card boxes.

(1) Results from RGB camera detects the edge of the card boxes

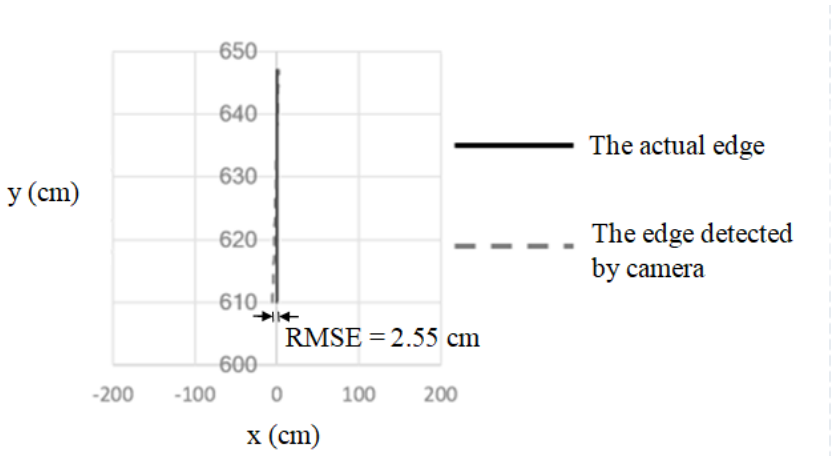

Figure 3.10 The actual edge of card boxes and the edge detected by RGB camera.

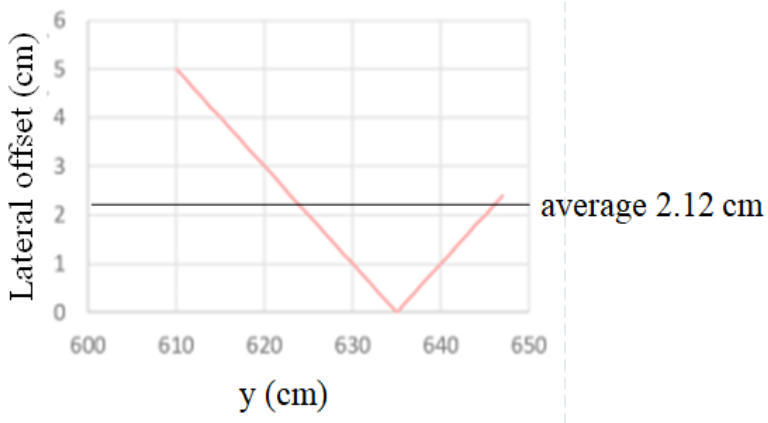

Figure 3.11 The lateral offset of edge detection by using an RGB camera.

From Figure 3.10 and Figure 3.11, it is shown that the Root Mean Square Error ($RMSE$) of the RGB camera edge detection system is equal 2.55 cm with an average lateral offset 2.12 cm. The $RMSE$ of the RGB camera edge detection system is rather high because the ROI of the input image is on the bottom of the image. Therefore, the distortion of the image should be considered. The distortion of the image will get higher if the ROI of the image is further from the center of the image.

(2) Results from the laser rangefinder detects the edge of the card boxes

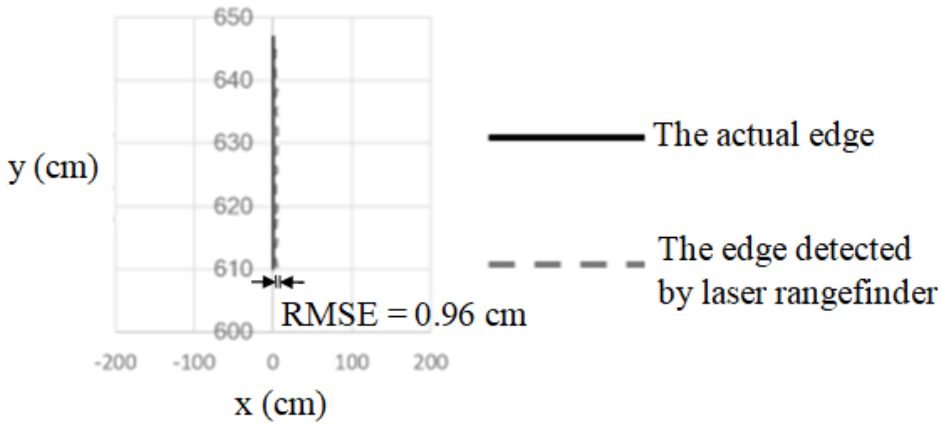

Figure 3.12 The actual edge of card boxes and the edge detected by laser rangefinder.

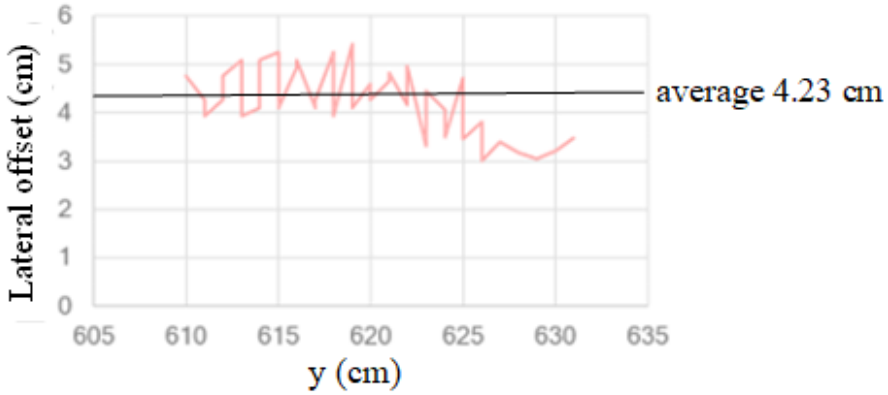

Figure 3.13 The lateral offset of edge detection by using a laser rangefinder.

From Figure 3.12 and Figure 3.13, it is shown that the $RMSE$ of the laser rangefinder edge detection system equal 0.96 cm with average of lateral offset 4.23 cm.

(3) Results from the sensor fusion detect the edge of the card boxes

In the simulation experiment, the percept was defined as the edge of the card boxes

1) Evidence a for feature is based on two descriptions: RGB camera (d^1), and laser rangefinder (d^2). (d^1) consists of a single feature: edge of box (d_1^1) and (d^2) consist of a single feature: edge of box (d_1^2). The belief for a feature is shown as below;

$$Bel_{d_1^1}^{s^1}|2^{\Omega}: (0.54, 0.33, 0.13)$$

$$Bel_{d_1^2}^{s^2}|2^{\Omega}: (0.52, 0.19, 0.29)$$

2) Evidence for a description: The belief for a description was transferred from the belief for a feature by using equation (3.19) with $r_{d^1} = \langle 1 \rangle \; and \; r_{d^2} = \langle 1 \rangle$. The belief for a description is shown as below;

$$Bel_{d^1}^{s^1}|2^{\Phi}: (0.54, 0.33, 0.13)$$

$$Bel_{d^2}^{s^2}|2^{\Phi}: (0.52,\ 0.19,\ 0.29)$$

3) Evidence for a percept: The belief for a percept was transferred from the belief for a description by using equation (3.20) with $r_p = \langle 1,1 \rangle$. The belief for a percept is shown as below;

$$Bel_p^{d^1 s^1}|2^{\Theta}: (0.54, 0.33, 0.13)$$

$$Bel_p^{d^2 s^2}|2^{\Theta}: (0.52,\ 0.19,\ 0.29)$$

The final belief function for percept can be estimated by using Dempster's rule combination. Equation (3.21) shows the combination between $Bel_p^{d^1 s^1}$ and $Bel_p^{d^2 s^2}$.

$$Bel_p = \left(Bel_p^{d^1 s^1} \oplus Bel_p^{d^2 s^2}\right) \tag{3.21}$$

The result of applying equation (3.10) to equation (3.21) is shown as below.

	$m(p^2) = 0.52$	$m(\overline{p^2}) = 0.19$	$m(\Theta) = 0.29$
$m(p^1) = 0.54$	0.28	0.10	0.16
$m(\overline{p^1}) = 0.33$	0.17	0.06	0.10
$m(\Theta) = 0.13$	0.07	0.02	0.04

$$m(p) = \frac{0.28 + 0.07 + 0.16}{1 - (0.17 + 0.10)} = 0.70$$
$$m(\bar{p}) = \frac{0.06 + 0.02 + 0.10}{1 - (0.17 + 0.10)} = 0.25$$
$$m(\Theta) = 1 - \ m(p) - m(\bar{p}) = 0.0.5$$

The probability mass for percept $(m(p))$ equals 0.7, which means that the observation from both sensors is certain.

Using equation (3.11) to calculate the weight of conflict metric (Con) which gives as a result, (Con) equal to 0.14.

Then, by integrating the characteristic of the laser rangefinder and machine vision, the result is shown as below.

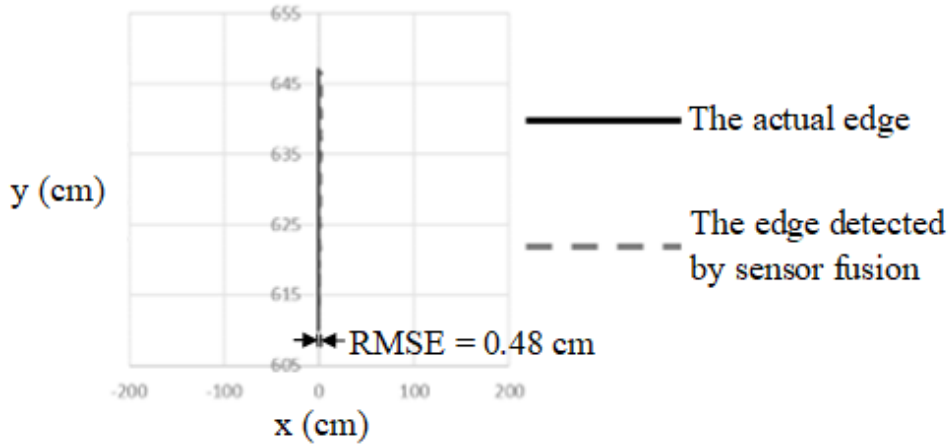

Figure 3.14 The actual edge of card boxes and the edge detected by sensor fusion.

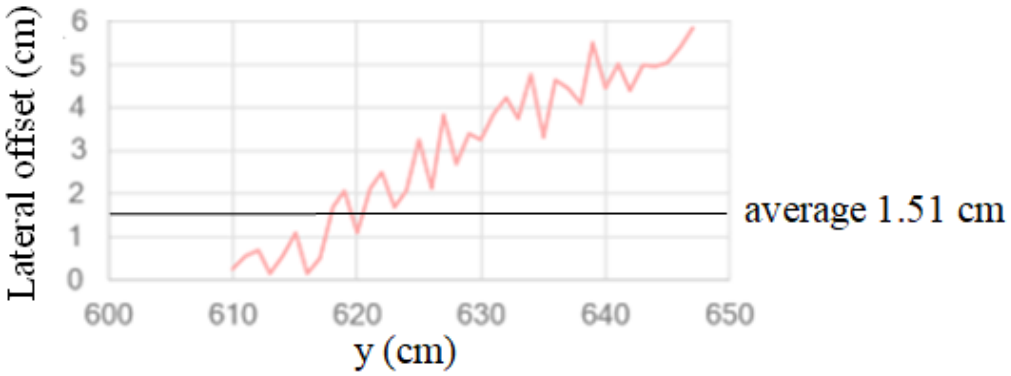

Figure 3.15 The lateral offset of edge detection by using sensor fusion.

Figure 3.14 and Figure 3.15 show the $RMSE$ of edge detection by using sensor fusion equal 0.48 cm with average of the lateral offset 1.51 cm.

3.4 Conclusion

In this chapter, to deal with the sensor's uncertainty, three theories of sensor fusion were studied. From the study about sensor fusion method, Dempster-Shafer theory was selected

as the sensor fusion method for this study because the prior probability distribution is not a requirement of Dempster-Shafer theory because in the real-time guidance, there is unknown prior probability distribution. The card boxes were used to simulate as crops in the simulation experiment. The simulation experiment was separated into three parts; the RGB camera detects the edge of the card boxes, the laser rangefinder detects the edge of the card boxes, and the sensor fusion detects the edge of the card boxes.

To combine the characteristics of both sensors, the Dempster-Shafer theory was used in the SFX architecture. The results show that the observation of both sensors is certain with the probability mass for percept equal to 0.70 and the weight of conflict equal to 0.14. The probability mass for percept equal to 0.70 means the observation of the sensor fusion detection of the edge of the card boxes is certain. However, it is not suitable to use the probability function for the practical application like the operation of an automatic combine harvester. Therefore, the further experiment and evaluation is necessary to develop a positioning system for an automatic combine harvester.

CHAPTER 4
PERFORMANCE OF QUASI-ZENITH SATELLITE SYSTEM FOR A COMBINE HARVESTER UNDER STATIC CONDITIONS

4.1 Introduction

The development of the QZSS and its receiver allowed to utilize the CLAS and MADOCA positioning augmentation system. From the literature review, both CLAS and MADOCA positioning augmentation systems have a good accuracy which has a potential to be utilized for a positioning system of an automatic combine harvester. Therefore, the purpose of this chapter is to evaluate the performance of QZSS for a combine harvester under static condition.

This chapter described the experiments methodology. The terminology of each parameter used for the performance evaluation under static conditions is included. The results of the performance of QZSS for a combine harvester under static conditions were presented and discussed.

4.2 Materials and methods

The experiments to evaluate the performance of the QZSS for a combine harvester under static conditions were conducted at the experimental farm of Hokkaido University under an open sky environment, which means there were no sight-blocking tall buildings or trees between June of 2019 and January of 2020. Figure 4.1 shows the setup for the experiment. This simple procedure guarantees that the three different GNSS systems are measuring the exact same position. Figure 4.2 shows the experimental location which was an old tennis court. Each one of the receivers was tested individually using their own antenna meaning that no GNSS splitter was used to obtain the signal from a single antenna into two or more receivers. The receiver antennas were mounted on a tripod stand at a height of 1.2 m above

the ground surface. One post hole of the tennis was used as a ground landmark. For each experiment, a brass plumb bob was used to set the tripod in the exact same central position of the landmark. The outputs of each GNSS system were logged in a PC at the rate of 10 Hz. The experiment took six hours. Starting at 10:00 and finishing at 16:00 (UTC +9 Time).

Figure 4.1 The setup of performance evaluation under static conditions.

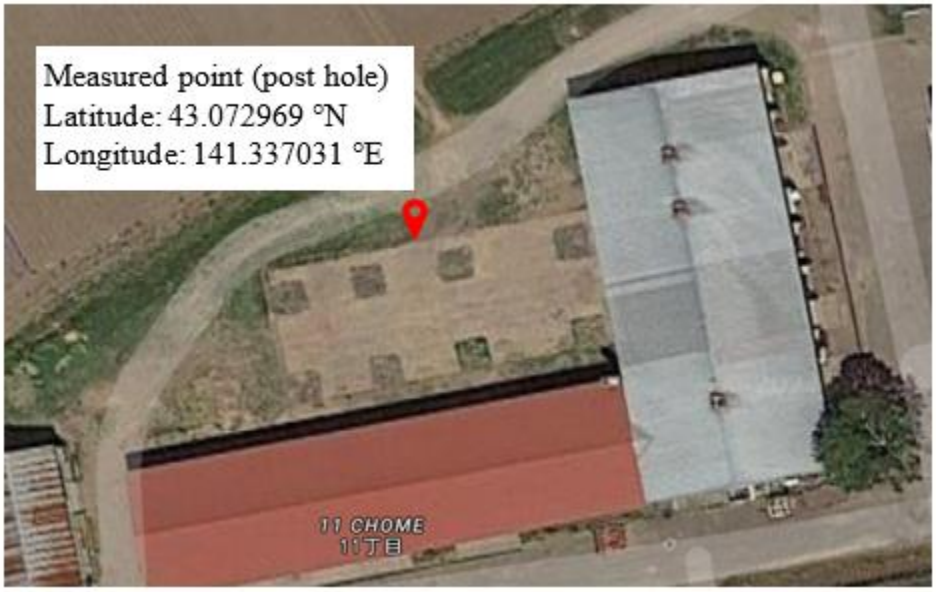

Figure 4.2 The experimental location for performance evaluation under static conditions.

4.2.1 The activation time and the reactivation time

A simple activation test was performed on each of the receivers at the experimental location before the experiment under static conditions. The test consisted of powering on each receiver and recording the convergency time; this means, the time each receiver takes to achieve its RTK fixed status. Please note that the Magellan MJ-3008-GM4-QZS receiver can only achieve RTK float status when using the MADOCA positioning augmentation system .

An additional reactivation time test was also performed. This test consisted of disconnecting the receiver antenna, waiting for the positioning signal to drop and then reconnecting the receiver antenna, waiting for the receiver to achieve its enhanced positioning status after this antenna disconnection and reconnection was also recorded. This test relevant because sometimes in field conditions the GNSS signal might drop due to external factors, so it is necessary to know an estimation of how much time does the receiver needs to recover from a sudden signal loss.

The time of the activation tests and the reconnection tests was recorded using the timestamp from the PC and it was estimated from the average of ten different measurements. The standard deviation, and the minimum and maximum values were calculated and helped to verify that measuring more times would not evidence any different behavior. Please note that the receiver using the CLAS positioning augmentation system cannot achieve RTK fixed status automatically after disconnecting the antenna or after powering on the receiver, it needs to be set up manually again. Therefore, the reactivation time is omitted because it would be the same as the activation time.

4.2.2 2DRMS and CEP

There are different methods for determining the accuracy of a GNSS under static conditions (Petrovski and Tsuiiji, 2012). The most used are the Twice Distance Root Mean Square ($2DRMS$) and the Circular Error Probability (CEP).

The $2DRMS$ accuracy indicates that the measured position will be within the stated distance from the true position 95% of the time. It is given by equation (4.1)

$$2DRMS = \sqrt{(\sigma_E^2 + \sigma_N^2)} \tag{4.1}$$

Where; σ_E is the standard deviation of the easting values

σ_N is the standard deviation of the northing values

The CEP is the radius of a circle containing 50% of the horizontal position measurement reported by the GNSS receiver. It is given by equation (4.2)

$$CEP = 0.59(\sigma_E + \sigma_N) \tag{4.2}$$

The $2DRMS$ and CEP are good accuracy estimators while using them to measure position points which have normal distribution towards a central point. (Droso et al., 2011). However, they require an additional accuracy estimator to incorporate accuracy into them which will be explained below.

4.2.3 RMSE

The $RMSE$ was used to incorporate accuracy into the $2DRMS$ and CEP by using $RMSE$ to describe the accuracy by measuring the errors between the GNSS data and the actual position (Rodriduez-Pérez et al., 2006). The position measured by the Trimble SPS855 GNSS receiver which utilize the RTK position augmentation system was used as the mean position. The $RMSE$ is given by equation (4.3)

$$RMSE = \sqrt{\frac{1}{n}\sum_{i=1}^{n}\left(E_i - \overline{E}\right)^2} \tag{4.3}$$

Where; E_i is the location of the i_{th} measurement along the easting and northing directions.

$\overline{E}$ is the mean of the measurements.

n is the total number of measurements.

4.3 Result and discussion

Table 4.1 shows the results of the ten measurements of the activation time and the reactivation time of each positioning augmentation system on the different date. The minimum values, maximum values, average values, and the standard deviation are calculated and also shown in Table 4.1. The results from the ten measurements of each positioning augmentation system shows they were almost the same. And the minimum and maximum values show a difference of around 1 second. With the standard deviation around 0.5; meaning the values tend to be close to the mean of the data. Therefore, it is acceptable to use the average time for comparison purposes.

Table 4.1 The activation and the reactivation time results.

Test Number	RTK (Real-time Kinematic) (2019/06/25)		MADOCA (2019/07/08)		CLAS (2020/01/16)	
	Act. time (s)	React. time(s)	Act. time (s)	React. time(s)	Act. time (s)	React. time(s)
1	13.9	13.4	31.5	43.7	127.1	-
2	15.1	12.5	30.2	42.8	128.4	-
3	13.7	12.3	29.5	43.7	128.5	-
4	14.3	13.2	29.2	43.3	129.1	-
5	14.2	12.7	30.8	43.9	128.3	-
6	14.7	12.8	31.1	42.4	127.6	-
7	14.1	13.1	30.7	43.1	128.3	-
8	14.0	12.4	30.5	44.2	128.6	-
9	13.8	12.9	30.1	42.7	127.3	-
10	14.6	13.5	29.7	43.5	128.1	-
Min.	13.7	12.3	29.2	42.4	127.1	-
Max.	15.1	13.5	31.5	44.2	129.1	-
Average	14.2	12.9	30.3	43.3	128.1	-
S.D.	0.44	0.42	0.73	0.58	0.62	-

From Table 4.1, it can be seen that the activation time of the RTK positioning augmentation system; meaning the time necessary to achieve RTK fixed status on average in 14.2 seconds. For the MADOCA positioning augmentation system, it can achieve RTK float in 30 seconds on average, which means this is a short activation time considering that while using the MADOCA mode, the receiver does not require an NTRIP service provider. In contrast, the CLAS positioning augmentation system could achieve RTK fixed status a little slower, which took 128 seconds on average.

In case of the reactivation time from Table 4.1, the RTK and MADOCA positioning augmentation systems performed similar times comparing to its own activation time. On the other hand, the CLAS positioning augmentation system cannot achieve RTK fixed status automatically after disconnecting and reconnecting the antenna, the manual set up needs to be done. Therefore, the reactivation of the CLAS positioning augmentation system is omitted in Table 4.1 because it would be similar to the activation time.

The results from Table 4.1 show that the activation times of three positioning augmentation systems are not too much different. These results imply that it would take less than 3 minutes while utilizing them with an automatic combine harvester, even though there might be some special cases caused by some abnormal factors such as geography or weather conditions that cause to have any of these positioning augmentation system be ready in more time.

As mentioned before in the experimental methodology, the RTK positioning augmentation system is used as the reference for comparison purpose. Therefore, the RTK variations should be analyzed because even the RTK positioning system might show small variations in position over time (Rodriduez-Pérez et al., 2006). This analysis is needed to clarify whether variations during the experiment are caused by variation of the RTK reference or caused by the variations in the CLAS or MADOCA positioning augmentation system.

Figure 4.3 shows the result from the performance evaluation under static conditions of the RTK positioning augmentation system. It is easier to visualize the distance in meters than in degrees. Therefore, the result in Figure 4.3 is plotted in Universal Transverse Mercator (UTM) coordinates instead of latitude longitude coordinates. The position points measured by the RTK positioning augmentation system are scattered over a small area about 0.05 m by 0.06 m.

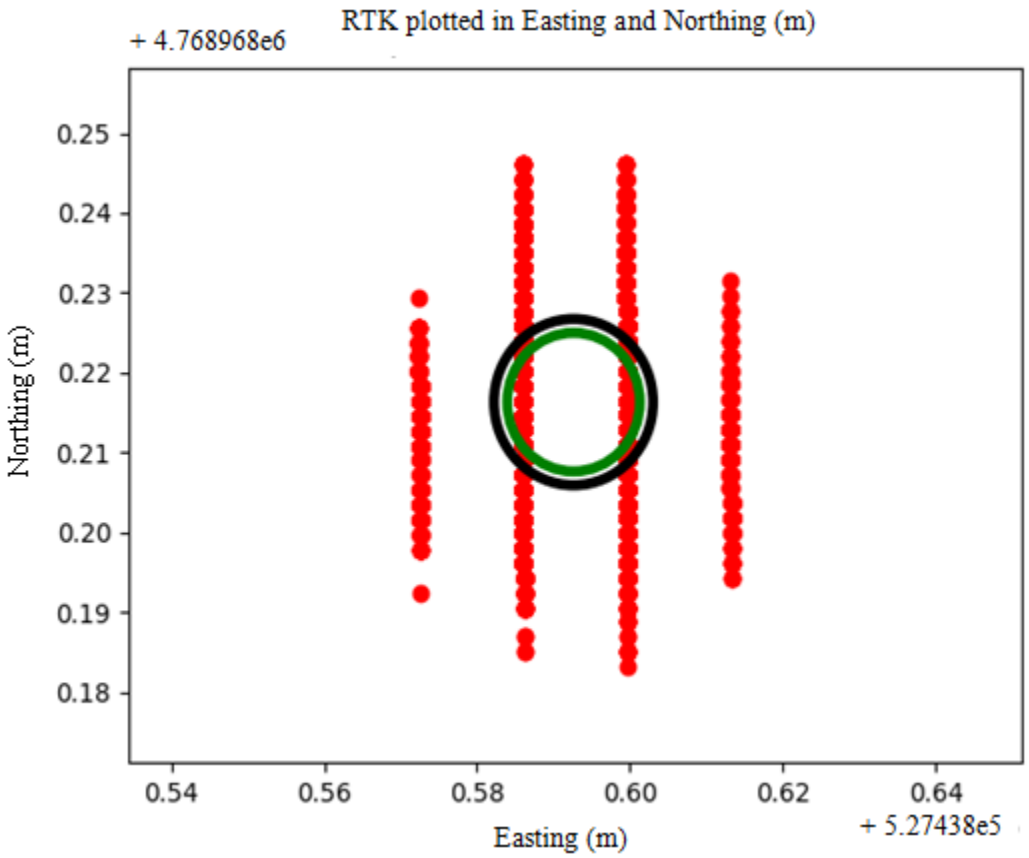

Figure 4.3 Result from the performance evaluation under static conditions of the RTK positioning augmentation system plotted in Easting and Northing coordinates.

Figure 4.4 shows the variations of the RTK positioning augmentation system over time. However, to neglect these variations in position overtime, it is possible to use the mean of logged positions measured by the RTK positioning augmentation system as an origin point for the reference in order to compare with either CLAS or MADOCA positioning augmentation system.

The small scattered area of the logged points measured by the RTK positioning augmentation system in Figure 4.3 and the small variations in position over time in Figure 4.4 verify that it is possible to use the mean of logged positions measured by the RTK

positioning augmentation system to neglect these small variations while using the positions measured by the RTK positioning augmentation system as a reference.

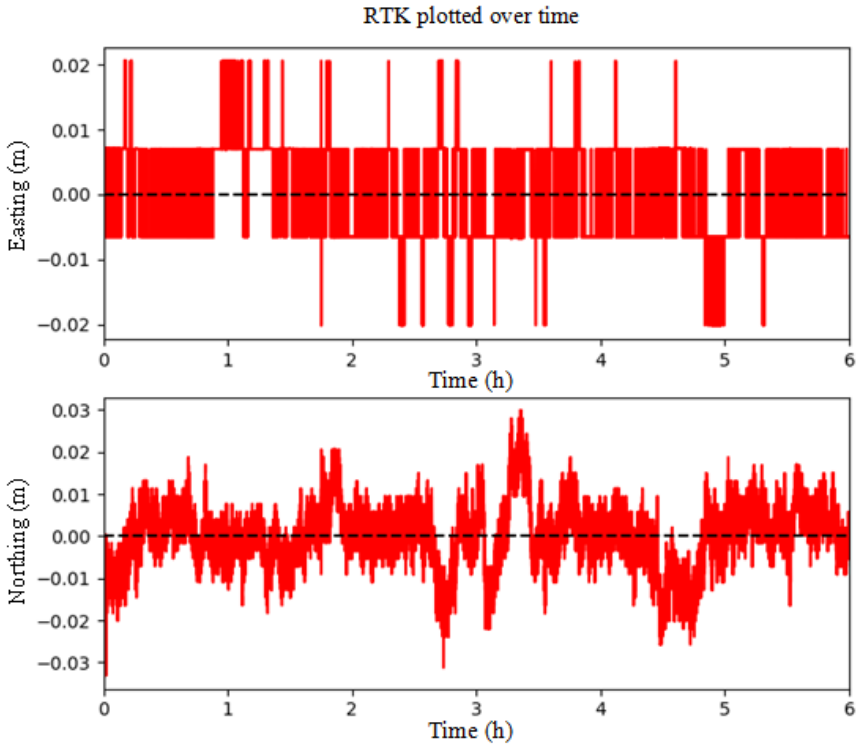

Figure 4.4 Result from the performance evaluation under static conditions of the RTK positioning augmentation system plotted in time series.

By using equation (4.1) and equation (4.2), the $2DRMS$ and the CEP can be calculated, respectively. Figure 4.3, Figure 4.5, and Figure 4.6 show the $2DRMS$ which is measured within the black circle and the CEP which is the radius of the green circle in the plot.

Figure 4.5 and Figure 4.6 present an overview of the performance evaluation of the QZSS under static conditions. The plots are shown in UTM coordinates and the origin point (0,0) is the mean of the logged positions measured by the RTK positioning augmentation system. As mentioned before, the purpose of using this mean of logged positions is to neglect small

variations in positions overtime. The mean of logged positions and the positions points measured by the CLAS and MADOCA positioning augmentation system are displayed by the blue points and the cloud of red points, respectively.

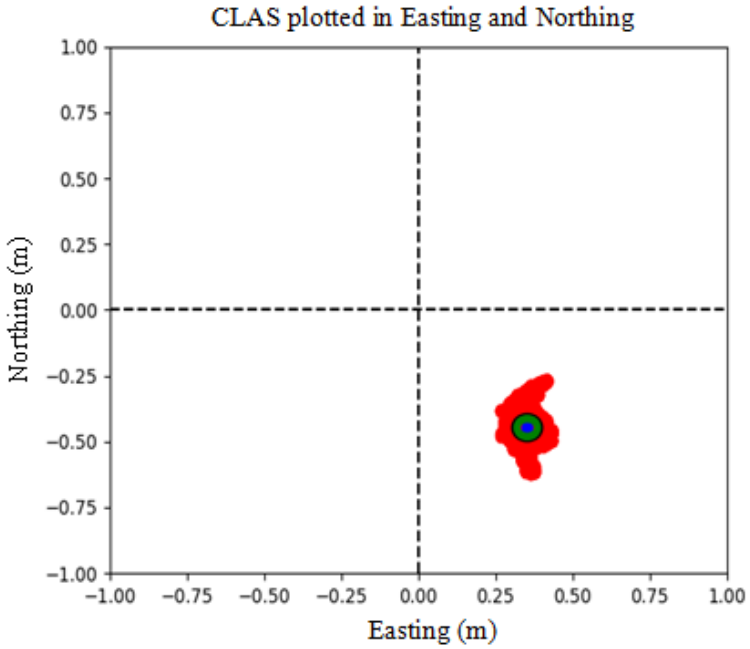

Figure 4.5 Result from the performance evaluation under static conditions of the CLAS positioning augmentation system plotted in Easting and Northing coordinates.

From the Figure 4.5, the position points measured by the CLAS positioning augmentation system are uniformly grouped and scattered over an area around 0.25 m by 0.50 m. The mean position or the blue point located in the center of the cloud of red points shows small instabilities or the sudden oscillations.

Figure 4.6 shows that the positions measured by the MADOCA positioning augmentation system are scattered over an area of about 0.70 m by 0.70 m and display a loop inside this area. This loop indicates the instability of the MADOCA positioning augmentation system.

However, the mean position or the blue point which locates inside the area where the cloud of red points are dense, which means this positioning augmentation system has a good accuracy but it is not good as the mean position of the CLAS positioning augmentation system.

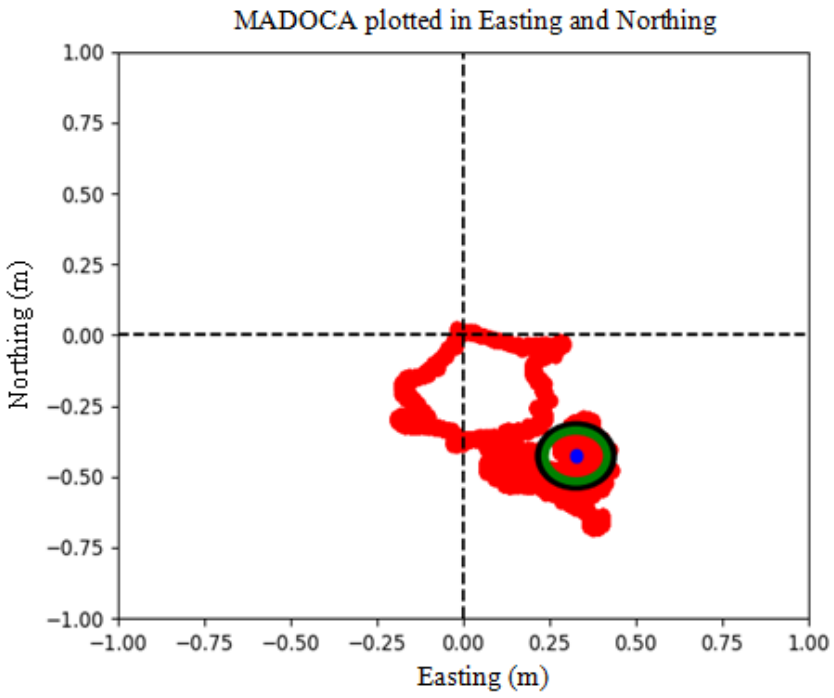

Figure 4.6 Result from the performance evaluation under static conditions of the MADOCA positioning augmentation system plotted in Easting and Northing coordinates.

The result shown in Figure 4.5 give an inference that the accuracy of the CLAS positioning augmentation system is better than the accuracy of the MADOCA positioning augmentation system. The loop in the plot of the MADOCA positioning augmentation system shown in Figure 4.6 gives the initial idea that an oscillation in the measured coordinates might cause this loop until they converge and scatter over area of about 0.50 m by 0.50 m.

The $2DRMS$ and the CEP circle of the CLAS positioning augmentation system shown in Figure 4.5 is smaller than the MADOCA positioning augmentation system shown in Figure 4.6. This is an expected result caused by the size of the area of the cloud of red points in Figure 4.5 and Figure 4.6.

Table 4.2 Accuracy analysis under static conditions

Positioning augmentation system	**2DRMS (m)**	**CEP (m)**	**Number of satellites**	**N-S offset (m)**	**E-W offset (m)**	**RMSE (m)**
RTK	0.010	0.008	14.6	Reference	Reference	Reference
CLAS	0.041	0.034	11.0	-0.447	0.352	0.57
MADOCA	0.107	0.089	12.7	-0.427	0.326	0.54

The $2DRMS$, the CEP and the average number of satellites tracked during the experiment for each one of the position augmentation systems were listed in Table 4.2. The results show that the CLAS positioning augmentation system has a rationally small $2DRMS$ and CEP; even though they are around four times bigger than the results from the RTK positioning augmentation system which are still less than 0.05 m. On the other hand, the $2DRMS$ and CEP of MADOCA positioning augmentation system are ten times bigger than the results from the RTK positioning augmentation system.

In terms of the $2DRMS$ and CEP, a big value refers to most of the position points scattered over a wider area, while a smaller value refers to the concentration of the position points within a small area.

The results from Table 4.2 support the inference obtained from Figure 4.7 and Figure 4.8; the CLAS positioning augmentation system is more accurate than the MADOCA positioning augmentation system. An indication of the quality of the signal reception can be interfered from the average number of satellites tracked. The receiver or user's location and time can

be estimated by a minimum of four satellites (Fan et al., 2019) meaning the more satellites used, the greater the solution quality and integrity. This conclusion is necessary as an estimator for the experiments because it can help with the perception in case of the accuracy of any positioning augmentation system is affected by weather conditions, or the satellites line of view, or the accuracy is just inferior. From the results of the experiments, even though the CLAS positioning augmentation system registered on average less satellites than the MADOCA positioning augmentation system, it could perform better. This means the inferior accuracy of the MADOCA positioning augmentation system was not caused by the lack of satellites, it was caused by the inherent measurement principle of the system.

Additionally, to describe the accuracy by measuring the errors between each receiver position data and the actual position, the $RMSE$ was calculated by using equation (4.3). As mentioned before, the mean of the logged positions measured by the RTK positioning augmentation system was used as the origin points (0,0) in Figure 4.5 and Figure 4.6. The difference between each result of the CLAS or MADOCA positioning augmentation system and the result of the RTK positioning augmentation system is termed as the bias of each receiver. The mean of the bias values within a period is termed as the offset of each receiver (Wang and Noguchi, 2019). This offset is calculated from the easting and northing coordinates separately and shown in Table 4.2 with the $RMSE$ value. The offset from Table 4.2 shows that both CLAS and MADOCA positioning augmentation system have a similar offset of around 0.33 m and 0.43 m in the easting and northing coordinates, respectively. The $RMSE$ of both system is around 0.55 m. These results are different from the results of $2DRMS$ and CEP which could imply that the MADOCA positioning augmentation system is as accurate as the CLAS positioning augmentation system in terms of a constant bias.

However, Figure 4.5 and Figure 4.6 provides only an idea of the static positioning experiment without behaviors over time. Table 4.2 does not provide information for a specific time, it summarized only the data of the $2DRMS$, CEP, offset, and $RMSE$; which give a good accuracy analysis for the total length of the performance evaluation under static conditions.

Therefore, Figure 4.7 and Figure 4.8 shows the logged position data measured by the CLAS and MADOCA positioning augmentation systems from the performance evaluation under static conditions plotted against time in easting and northing coordinates, respectively.

The results from Figure 4.7 show that the position data measured by the CLAS positioning augmentation system has a small oscillation of around 0.20 m in the northing coordinate during the first hour, then it becomes stable since the second hour until the end of the evaluation. On the other hand, the position data in the easting coordinate converges to an approximately constant value within a 0.10 m range and it is stable from the beginning until the end of the evaluation.

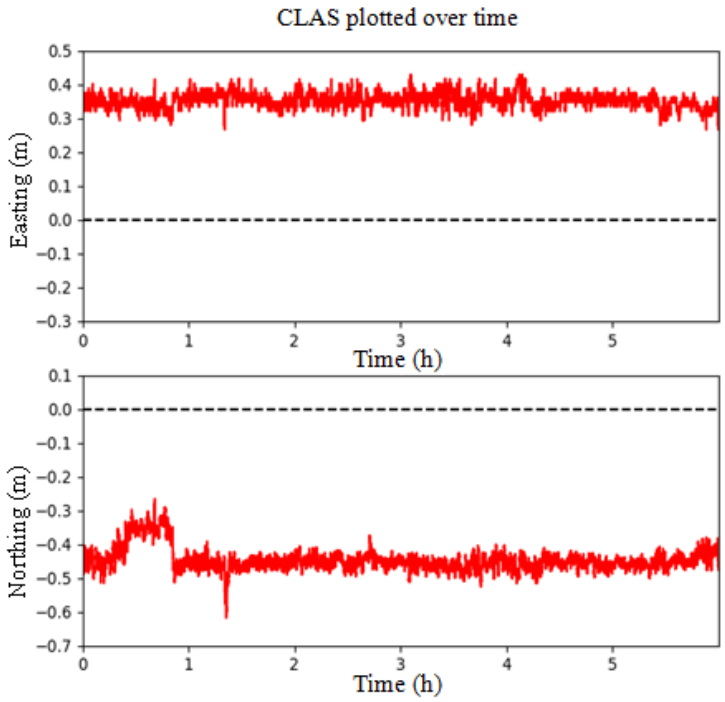

Figure 4.7 Result from the performance evaluation under static conditions of the CLAS positioning augmentation system plotted in time series.

The result from Figure 4.7 implies that the CLAS positioning augmentation system might be appropriate to utilize with the automatic combine harvester. Although the bias respect to the reference measured by the RTK positioning augmentation system is around 0.40 m, it seems to be almost constant during the six hours of the evaluation. Please note that there is a deviation of 0.20 m during the first hour of the CLAS positioning augmentation system in the northing coordinate. This deviation might be caused by an inherent characteristic of the CLAS positioning augmentation system.

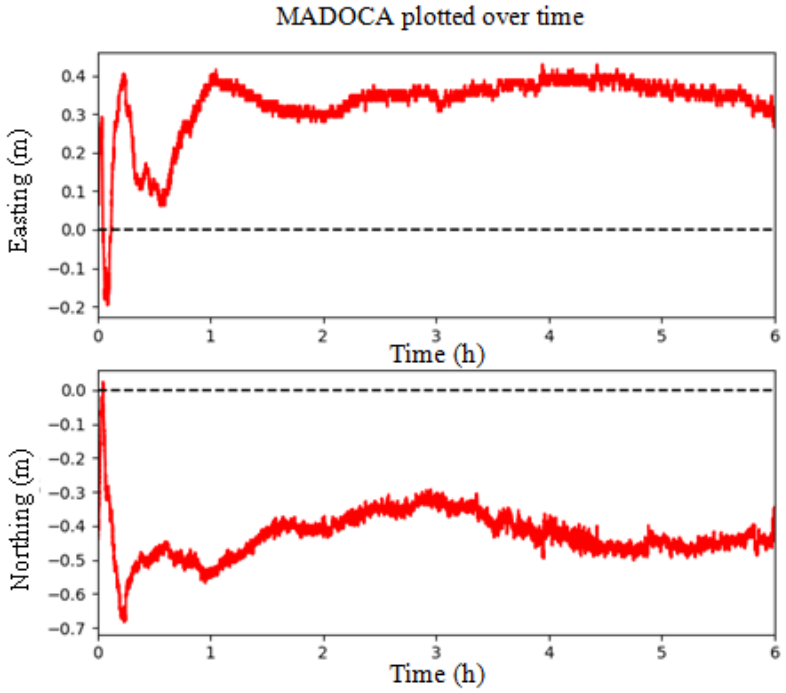

Figure 4.8 Result from the performance evaluation under static conditions of the MADOCA positioning augmentation system plotted in time series.

In contrast, the MADOCA positioning augmentation system has a different characteristic compared to the CLAS positioning augmentation system, as shown in Figure 4.8. There is a big oscillation of almost 0.70 m in both the easting and northing coordinates during the first hour of the evaluation. However, this oscillation gets smaller gradually since the second hour, then it becomes stable since the third hour and it starts to converge to a range of 0.20 m for

both the easting and northing coordinates. In terms of the bias with respect to the reference measured by the RTK positioning augmentation system, this bias is around 0.40 m. Compared to the CLAS positioning augmentation system, this bias is not constant during the six hours of the performance evaluation under static conditions. Therefore, it is not suitable to utilize the MADOCA positioning augmentation system to an automatic combine harvester during the first hour, meaning it might be used after waiting for an hour. However, the idea of a constant offset bias is not correct. This time restriction was considered in for the experiment to test the feasibility of an auto-guided combine harvester utilizing the MADOCA positioning augmentation system.

4.4 Conclusions

This chapter explained the experiment methodology to evaluate the performance of QZSS for a combine harvester under static conditions. The experiments were conducted in the open sky area. To guarantee that the three positioning augmentation systems in the experiment measure the exact same position, the receiver antennas were mounted on a tripod stand using a brass plumb bob to set the tripod in the exact same central position of the selected post hole as the landmark. The RTK positioning augmentation system was used as a reference for the evaluation.

Before beginning the experiments, a simple activation test was performed on each of the receivers at the experimental location. Then, an additional reactivation time test was also performed. The results showed that the average activation time of around 14.2 seconds, 128.1 seconds, and 30.3 seconds for the RTK, CLAS, and MADOCA positioning augmentation system, respectively. The average reactivation time was around 12.9 seconds and 43.3 seconds for the RTK and MADOCA positioning augmentation system, respectively. Please note that the CLAS could not achieve RTK fixed status for the reactivation time test and it can be omitted because it would be the same as the activation time.

The $2DRMS$, CEP, and $RMSE$ were calculated to evaluate the performance under static conditions. The results showed a $2DRMS$ of 0.04 m and 0.10 m, a CEP of 0.03 m and 0.08 m, and a $RMSE$ of 0.57 m and 0.54 m for the CLAS and MADOCA positioning augmentation system, respectively.

The results from the logged position data plotted against time showed the MADOCA had different characteristic compared to the CLAS positioning augmentation system. Although both positioning augmentation systems have relatively short activation times, the CLAS positioning augmentation system performed better under static conditions.

CHAPTER 5
FEASIBILITY OF AN AUTO-GUIDED COMBINE HARVESTER UTILIZING QUASI-ZENINTH SATELLITE SYSTEMS AS A NAVIGATION SENSOR

5.1 Introduction

According to the performance of the QZSS for a combine harvester under static conditions in Chapter 4, both CLAS and MADOCA positioning augmentation systems show a good performance; especially, the CLAS positioning augmentation system. Therefore, the purpose of this chapter is to test the feasibility while utilizing the QZSS as a navigation sensor for an auto-guided combine harvester.

This chapter explains the experiment methodology. The results of the experiments while utilizing the CLAS and MADOCA positioning augmentation systems as a navigation sensor for an auto-guided combine harvester are also presented and discussed.

5.2 Materials and methods

There are three tests to verify the feasibility while utilizing the QZSS as a navigation sensor for an auto-guided combine harvester. Figure 5.1 shows the overall setup for the three tests. The methodology for each test will be described as below.

The first test were conducted at the experimental farm of Hokkaido University in order to verify the feasibility of an auto-guided combine harvester utilizing the QZSS as a navigation sensor. The auto-guided combine harvester was equipped with the Magellan MJ-3008-GM4-QZS receiver connected directly to its own antenna without using a GNSS splitter. The auto-guided combine harvester ran along four paths of the pre-designed navigation map. This pre-designed navigation map consisted of a set position points in latitude and longitude

coordinates. In each run, the CLAS and MADOCA positioning augmentation systems were utilized as a navigation sensor. The purpose of this test is to verify the possibility of utilization of both CLAS and MADOCA positioning augmentation systems as a navigation sensor for the auto-guided combine harvester.

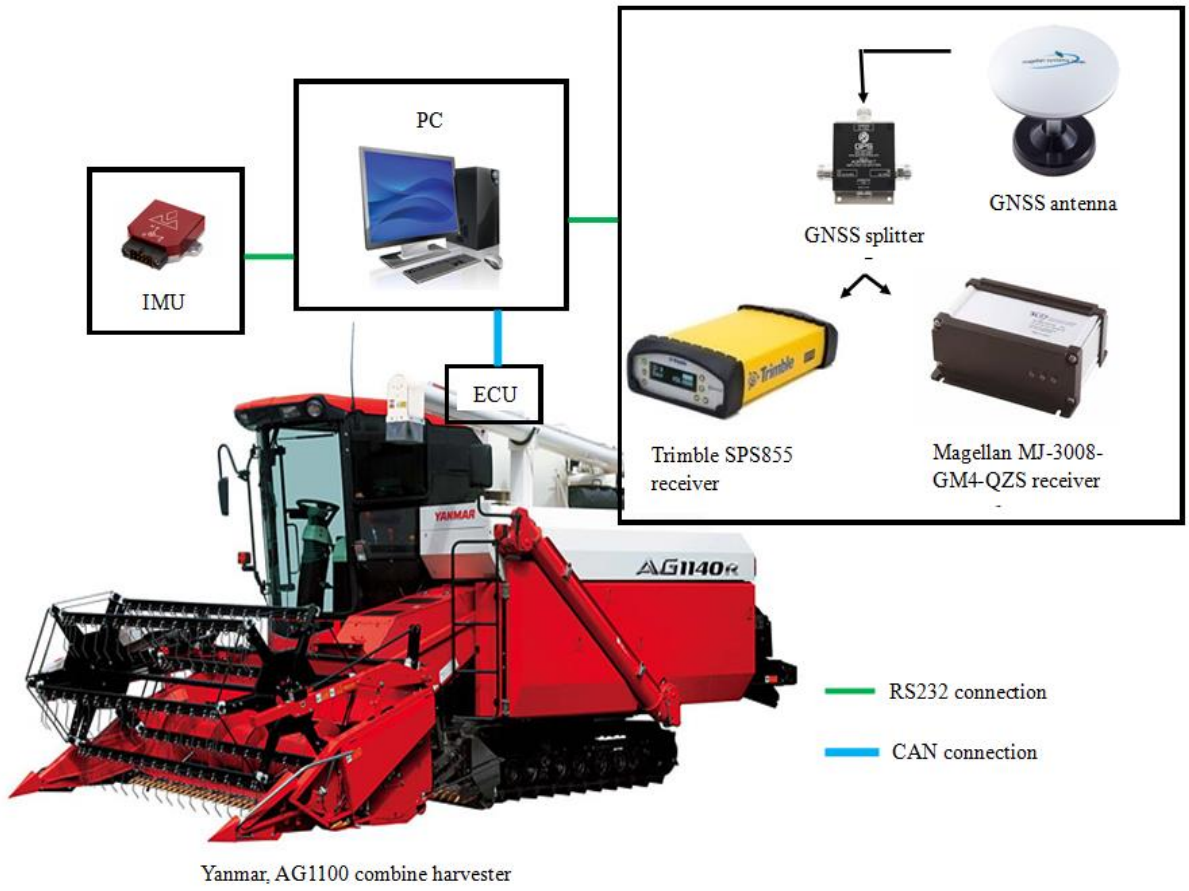

Figure 5.1 The overall setup of three feasibility tests.

The second test was performed by using the auto-guided combine harvester equipped with Trimble SPS855 receiver and the Magellan MJ-3008-GM4-QZS receiver. Both receivers were tested together using the antenna of the Magellan MJ-3008-GM4-QZS receiver via a GNSS splitter as shown in Figure 5.1. The auto guided combine harvester traveled one

straight path in the experimental farm with a constant velocity of 0.8 m/s by using the RTK positioning augmentation system as a navigation sensor. Four runs with two-hours interval on different date were performed. Each run took around 10 minutes while the outputs of both receivers were logged in a PC at the rate of 10 Hz. The reason of performing the test on different dates is because the Magellan MJ-3008-GM4-QZS receiver cannot utilize the CLAS and MADOCA position augmentation system simultaneously. The test on each day took 6 hours by activating the CLAS, MADOCA, and RTK positioning augmentation systems from 10:00 to 16:00 (UTC +9 Time) on different dates to evaluate the time dependency of each system. The $RMSE$ of the lateral deviation respect to the pre-designed navigation map was calculated by using equation (4.3). The lateral deviation was chosen to calculate the $RMSE$ and show it as the result of the test, because the straight path contained in the pre-designed navigation map works as the target position, and the positioning points logged by each positing augmentation system usually has some lateral deviation from this target position.

The purpose of the third test is to evaluate the performance of the CLAS and MADOCA augmentation systems as a navigation sensor for an auto-guided combine harvester. Similar to the second test, the test took 6 hours by activating the CLAS, MADOCA, and RTK positioning augmentation systems from 10:00 to 16:00 (UTC +9 Time) on different dates to evaluate the time dependency of each system. Then, the CLAS and MADOCA positioning augmentation systems were used as a navigation sensor for the auto-guided combine harvester. The auto-guided combine harvester ran along the same two paths of the pre-designed navigation map with two-hour intervals of time between each experimental run. The first run was tested immediately after the CLAS and MADOCA positioning augmentation systems were activated. The RTK positioning augmentation system was used to create the pre-designed navigation map. The output measured by the RTK positioning augmentation system was also logged in the PC for the evaluation purposes.

5.3 Result and discussion

By utilizing the CLAS and MADOCA as a navigation sensor for the auto-guided combine harvester, the results shown in Figure 5.2 and Figure 5.3 confirm that the auto-guided combine harvester could run along four paths of the pre-designed navigation map. In both Figure 5.2 and Figure 5.3, the dashed line displays the pre-designed navigation map. The solid blue line displays the traveling path of the auto-guided combine harvester by utilizing the CLAS and MADOCA positioning augmentation systems, respectively. Each test took about 20 minutes. However, a further feasibility test is necessary because it is difficult to estimate the accuracy of each positioning augmentation system as a navigation sensor for the auto-guided combine harvester.

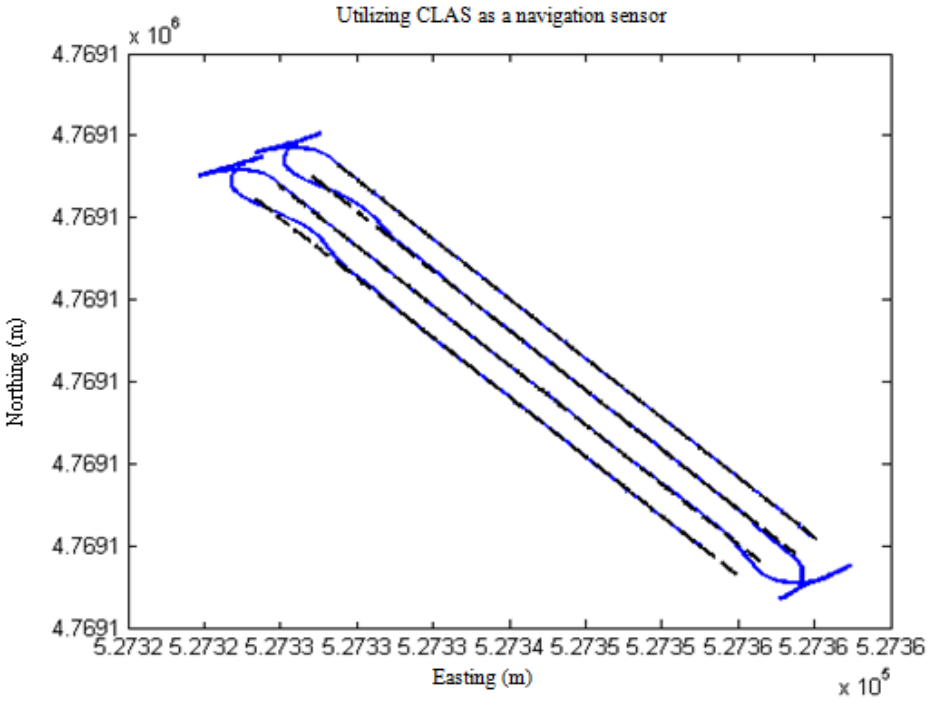

Figure 5.2 First feasibility test by utilizing the CLAS positioning augmentation system as a navigation sensor for the auto-guided combine harvester.

From Figure 5.2 and Figure 5.3, the results show that there are oscillations after the auto-guided combine harvester finishes the turning maneuver and enter the straight path. The cause of these oscillations is the utilization of the FDS with steering wheel for turning. However, the auto-guided combine harvester which utilizes the CLAS and MADOCA positioning augmentation system as a navigation sensor could return to the straight travel path along to the pre-designed navigation map, which gives an initial idea that utilizing either of these positioning augmentation systems as a navigation sensor for the auto-guided combine harvester is feasible.

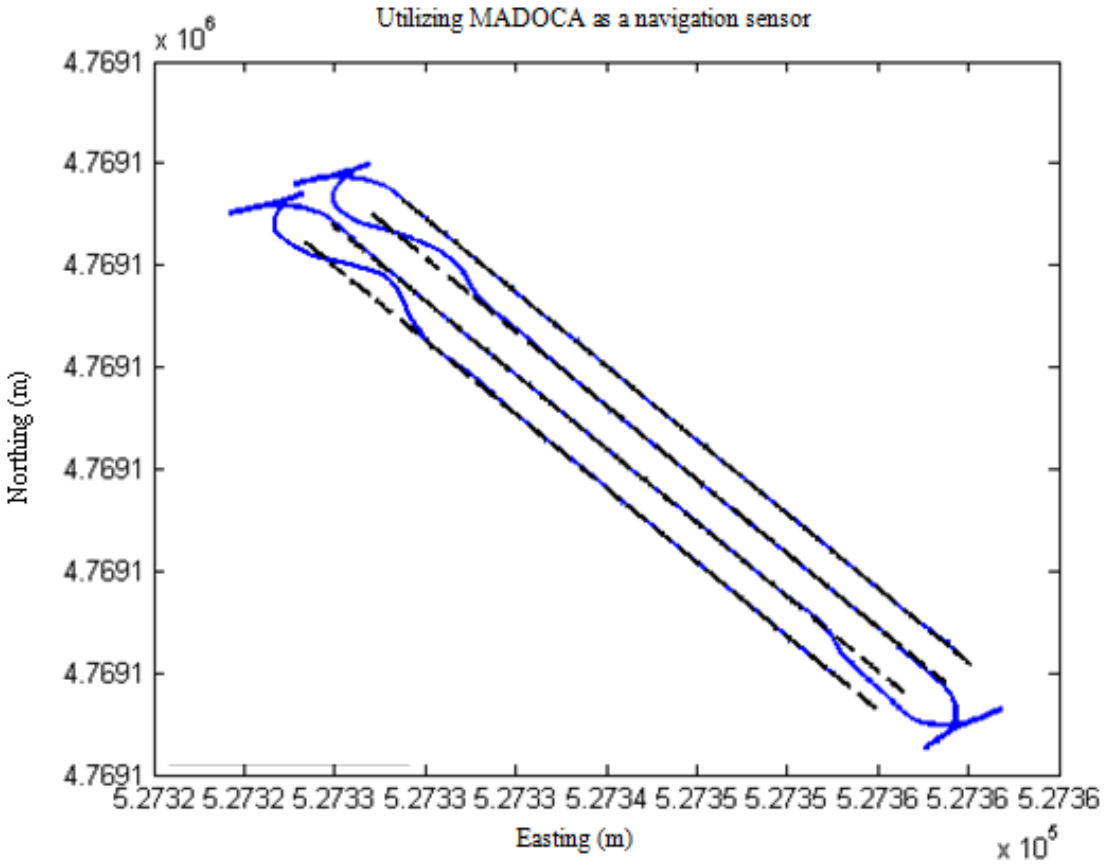

Figure 5.3 First feasibility test by utilizing the MADOCA positioning augmentation system as a navigation sensor for the auto-guided combine harvester.

Figure 5.4 and Figure 5.5 show the second feasibility test by utilizing the RTK positioning augmentation system as a navigation sensor for the auto-guided combine harvester logged with the CLAS and MADOCA positioning augmentation systems, respectively. In Figure 5.4 and Figure 5.5 the red lines represent the logged position data measured by the RTK positioning augmentation system, the black lines represent the pre-designed navigation map, and the blue lines represent the logged position data measured by the CLAS and MADOCA positioning augmentation systems, respectively.

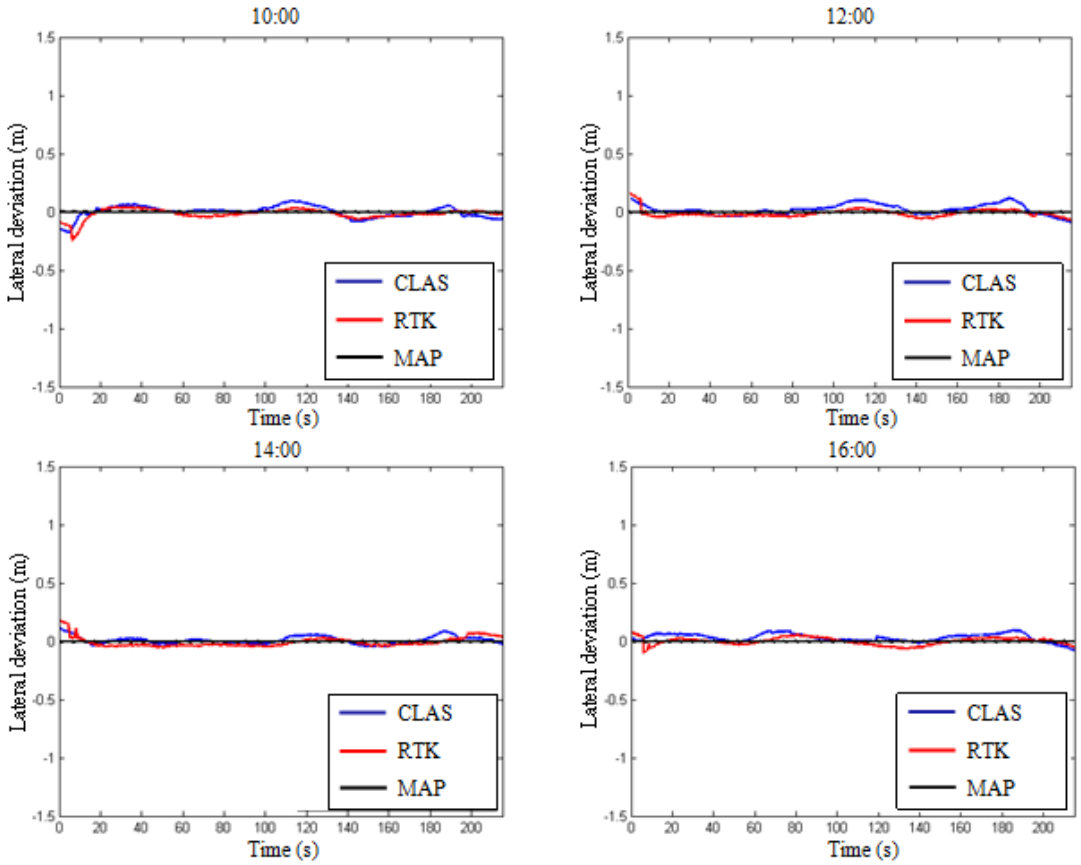

Figure 5.4 Second feasibility test by utilizing the RTK positioning augmentation system as a navigation sensor for the auto-guided combine harvester logged with the CLAS.

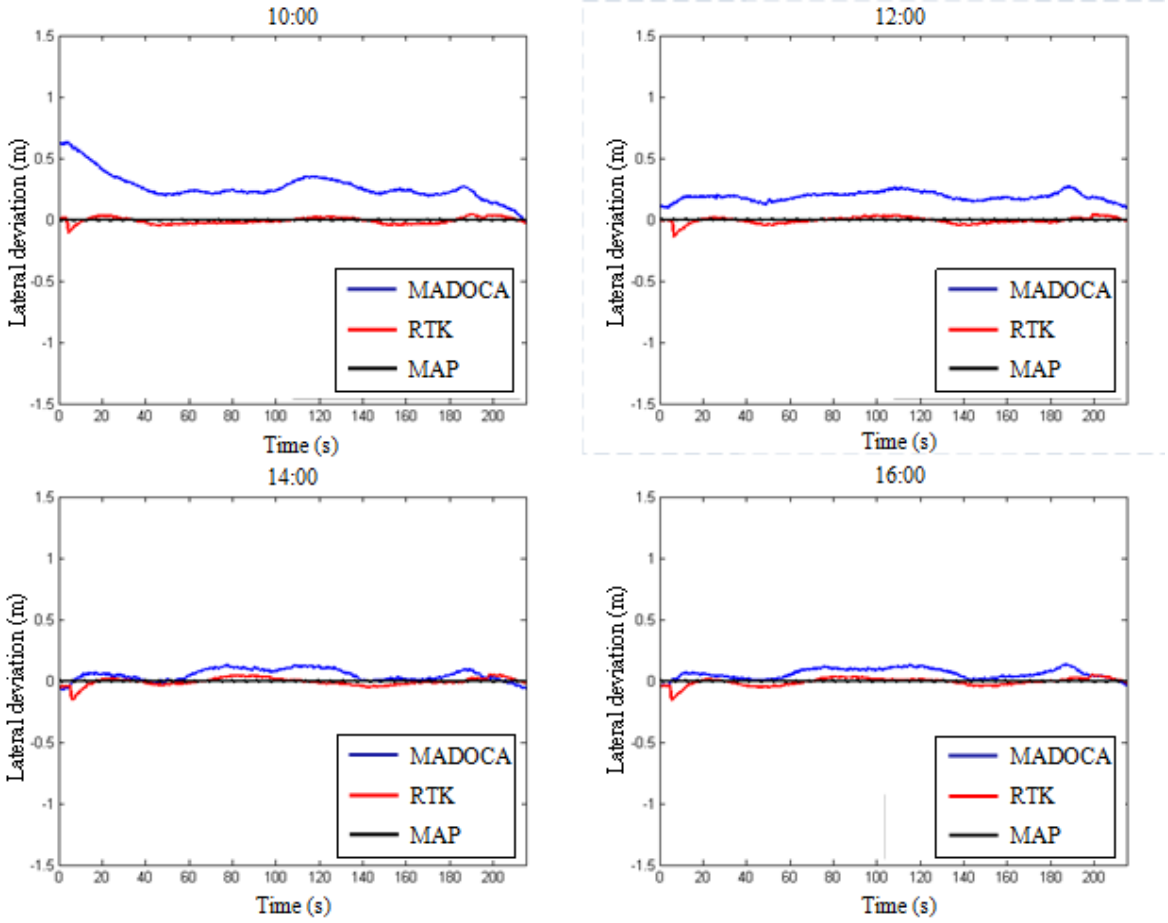

Figure 5.5 Second feasibility test by utilizing the RTK positioning augmentation system as a navigation sensor for the auto-guided combine harvester logged with the MADOCA.

Table 5.1 Results from second feasibility test with logged position measured by the CLAS.

Positioning augmentation system	**RMSE of lateral deviation (m)**			
	1st run at 10:00	**2nd run at 12:00**	**3rd run at 14:00**	**4th run at 16:00**
RTK	0.05	0.04	0.05	0.03
CLAS	0.06	0.05	0.04	0.05

Table 5.1 and Table 5.2 summarize the result from the second feasibility test. The lateral deviation was calculated from the difference between the pre-designed navigation map and the logged position data from the RTK, the CLAS, and the MADOCA positioning augmentation system. Please note that the straight path contained in the pre-designed navigation map serves as the target position, and the position points logged by each positioning augmentation system usually have some lateral deviation from the target position. By using equation (4.3), the $RMSE$ of the lateral deviation can be calculated. From Table 5.1, the comparison between the $RMSE$ of lateral deviation from the four runs shows that the RTK and the CLAS positioning augmentation system are stable, it is possible to state that for this test the CLAS positioning augmentation system might be as good as the RTK positioning augmentation system because it displays a $RMSE$ of lateral deviation less than 0.06 m.

Table 5.2 Results from second feasibility test with logged position measured by the MADOCA.

Positioning augmentation system	**RMSE of lateral deviation (m)**			
	1st run at 10:00	**2nd run at 12:00**	**3rd run at 14:00**	**4th run at 16:00**
RTK	0.03	0.03	0.04	0.04
MADOCA	0.32	0.18	0.06	0.07

However, results from Table 5.2 show that the MADOCA positioning augmentation system performance is poor for the first experimental run. An $RMSE$ of 0.32 m suggests that is not possible to use this positioning augmentation technique as a navigation sensor for the auto-guided combine harvester. The MADOCA positioning augmentation system performance improves in the second run and it gets better in the third run because the MADOCA positioning augmentation system requires at least two hours for stabilization, as evidenced in the data shown in Figure 4.8. Therefore, this positioning augmentation system is not suitable for the practical function as a navigation sensor of the auto-guided combine harvester. It is not practical to have an agricultural vehicle waiting in the field for two hours to complete

a harvest task that might take one hour for a small field. The results summarized in Table 5.1 and Table 5.2 are consistent to the result summarized in Table 4.2, and the data displayed in Figure 4.7 and Figure 4.8.

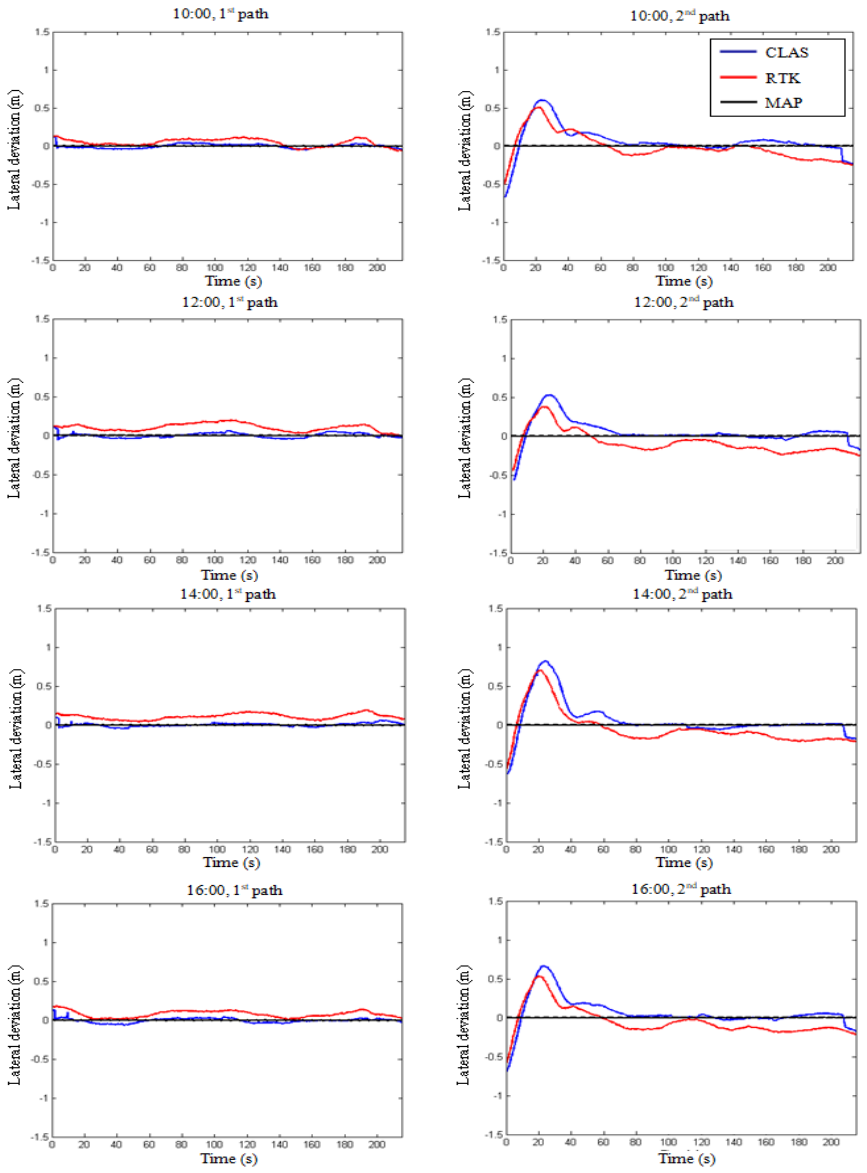

Figure 5.6 Third feasibility test by utilizing the CLAS positioning augmentation system as a navigation sensor for the auto-guided combine harvester logged with the RTK.

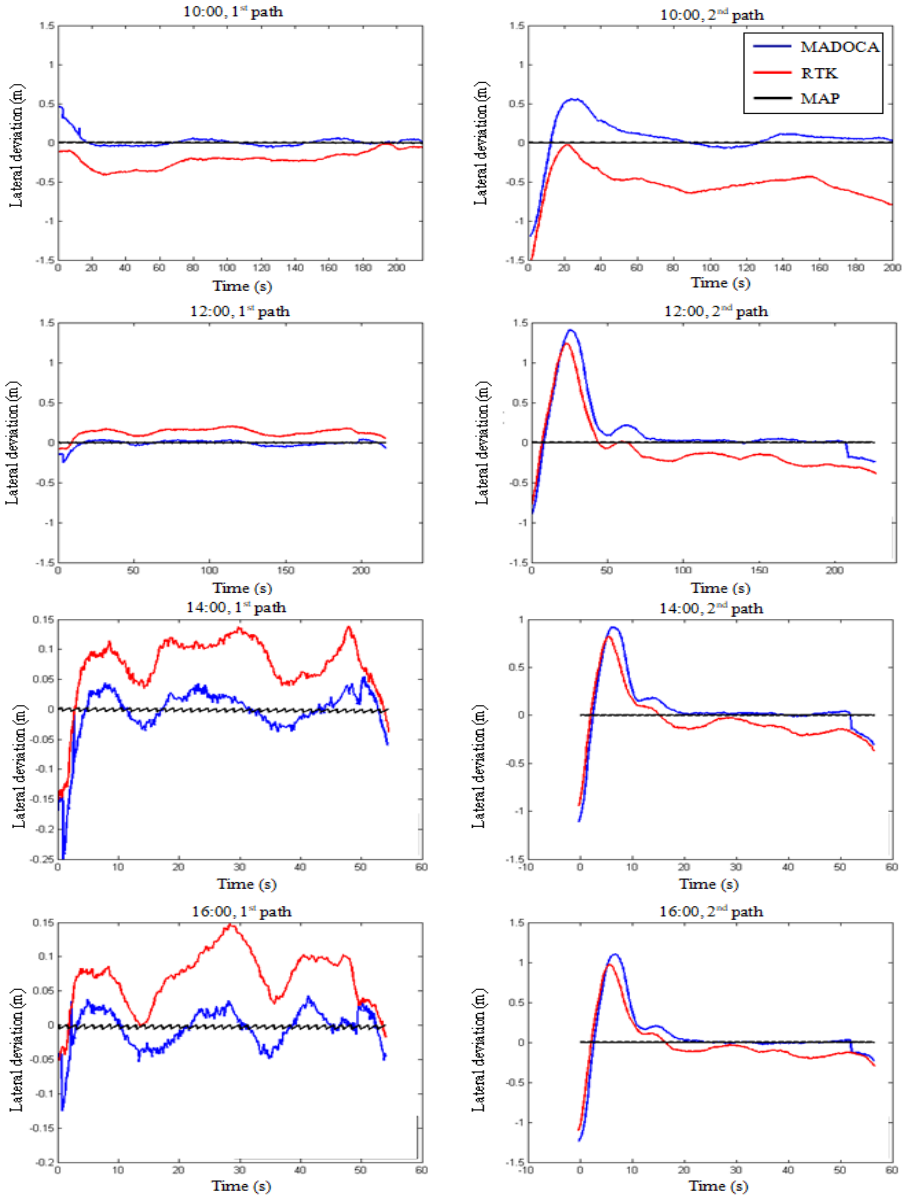

Figure 5.7 Third feasibility test by utilizing the MADOCA positioning augmentation system as a navigation sensor for the auto-guided combine harvester logged with the RTK.

Figure 5.6 and Figure 5.7 show the third feasibility test by utilizing the CLAS and MADOCA positioning augmentation as a navigation for the auto-guided combine harvester. The output measured by the RTK positioning augmentation system was also logged and is shown in

Figure 5.6 and Figure 5.7, as mentioned in the experiment methodology. In Figure 5.6 and Figure 5.7 the red lines represent the logged position data measured by the RTK positioning augmentation system, the black lines represent the pre-designed navigation map, and the blue lines represent the logged position data measured by the CLAS and MADOCA positioning augmentation systems, respectively.

Table 5.3 Results from third feasibility test by using the CLAS as a navigation sensor.

Positioning augmentation system	**RMSE of lateral deviation (m) from 1st path**				**RMSE of lateral deviation (m) from 2nd path**			
	10:00	**12:00**	**14:00**	**16:00**	**10:00**	**12:00**	**14:00**	**16:00**
CLAS	0.03	0.03	0.03	0.03	0.26	0.21	0.31	0.27
RTK	0.07	0.11	0.11	0.09	0.22	0.19	0.28	0.23

Table 5.3 summarizes the results from the third feasibility test by using the CLAS positioning augmentation system as a navigation sensor for the auto-guided combine harvester. The difference of the $RMSE$ of the lateral deviation between the CLAS positioning augmentation system and the RTK positioning augmentation system is almost constant since the time the experiment started; which means the position data navigated by the CLAS positioning augmentation system always converge to the position data measured by the RTK positioning augmentation system during the six hours of the experiment. Therefore, the CLAS positioning augmentation system does not have the time dependency phenomenon. The average $RMSE$ of the lateral deviation of the RTK positioning augmentation system for the actual path is 0.09 m and 0.23 m for the first path and second path, respectively. It is necessary to consider that when the auto-guided combine harvester performs a round trip, the width of the header used for harvesting requires a minimum distance between the going and the returning path. If this distance is too big, it might result in a gap of unharvested plants between the going and the returning path. This distance is defined as the overlap of the auto-guided combine harvester.

Table 5.4 Results from third feasibility test by using the MADOCA as a navigation sensor.

Positioning augmentation system	**RMSE of lateral deviation (m) from 1st path**				**RMSE of lateral deviation (m) from 2nd path**			
	10:00	**12:00**	**14:00**	**16:00**	**10:00**	**12:00**	**14:00**	**16:00**
MADOCA	0.11	0.04	0.07	0.08	0.36	0.69	0.63	0.67
RTK	0.23	0.09	0.08	0.09	0.58	0.66	0.58	0.66

Table 5.4 summarizes the results from the third feasibility test by using the MADOCA positioning augmentation system as a navigation sensor for the auto-guided combine harvester. The difference of the $RMSE$ of the lateral deviation between the results from the auto-guided combine harvester navigated by MADOCA positioning augmentation system and the RTK positioning augmentation system decreases drastically in the second run. It keeps decreasing in the third run and it is almost constant until the fourth run. Unlike the CLAS positioning augmentation system, the MADOCA positioning augmentation system has the time dependency phenomenon, according to the results from the performance evaluation under static conditions in Chapter 4 and the second feasibility test while using the RTK positioning augmentation system as a navigation sensor shown in Table 5.2 Although results from the performance evaluation under static conditions of the MADOCA positioning augmentation system in Chapter 4 suggest that it is necessary to wait 1 hour after activation before using it, the results from the third feasibility test suggest that it is necessary to wait 2 hours. Therefore, the MADOCA positioning augmentation system should be activated 2 hours before using it to navigate the auto-guided combine harvester for a safe and efficient work. The average $RMSE$ of the lateral deviation of the RTK positioning augmentation system or the actual path, after the MADOCA positioning augmentation system converges to the RTK positioning augmentation system, is 0.086 m and 0.63 m for the first path and second path, respectively.

Please note that the $RMSE$ values for the RTK positioning augmentation system in Table 5.3 and Table 5.4 are different because the robot combine harvester navigated using either CLAS

or MADOCA positioning augmentation systems. The RTK positioning augmentation system is only measuring the real position of the auto-guided combine harvester and it takes no part in the automatic navigation. From Table 5.3 and Table 5.4, it is not possible for the $RMSE$ values of the RTK positioning augmentation system to be too similar for both experiments, because that would mean that CLAS and MADOCA positioning augmentation system have almost the same accuracy.

Result summarized in Table 5.3 and Table 5.4 suggest that when using either the CLAS or MADOCA positioning augmentation system as a navigation sensor, it is necessary to consider the bias compensation for each augmentation system. The overlap between each path of the pre-designed navigation map should be set to 0.09 m when using either CLAS or MADOCA positioning augmentation system as a navigation sensor. However, this overlap should be updated periodically due to the earth's crustal movement for compensation of biases between the RTK positioning augmentation system and either CLAS or MADOCA positioning augmentation system.

The logged positions measured by the RTK positioning augmentation system shown in Figure 5.5 and Figure 5.6 by the red lines display a bigger bias respect to the pre-designed navigation map represented by the black lines in comparison to both CLAS and MADOCA positioning augmentation system used as navigation sensor for the auto-guided combine harvester. This is because the logged positions measured by the RTK positioning augmentation system are more accurate for both the static and dynamic positioning experiments. The auto-guided combine harvester tries to follow the pre-designed navigation map according to the position navigated by either CLAS or MADOCA positioning augmentation systems, but it cannot tell the difference between one or another respect to the real path. Therefore, the logged positions measured by the RTK positioning augmentation system represent the actual path that the robot combine harvester ran. The logged positions data from the second path were logged after finishing the turning maneuver of the first path.

It can be observed in Figure 5.6 that by using the CLAS positioning augmentation system as a navigation sensor, the position data provided by the CLAS converges to almost the same position data provided by the RTK positioning augmentation system. In contrast, the positioning data navigated by the MADOCA positioning augmentation system from Figure 5.7 diverges considerably respect to the position data provided by the RTK positioning augmentation system while using the MADOCA positioning augmentation system as a navigation sensor. This situation occurs because the MADOCA position augmentation system is a time dependent system; which means it requires several hours to achieve an acceptable control performance. The lateral deviation was calculated by the comparison between the map points and the logged position data from each positioning augmentation system and the RTK positioning augmentation system. Therefore, the CLAS and the RTK positioning augmentation system have a smaller $RMSE$ of the lateral deviation in comparison to the MADOCA and the RTK positioning augmentation system.

Considering the bias observed in Figure 5.6 and the data summarized in Table 5.1, it is possible to conclude that the $RMSE$ of the lateral deviation of the CLAS positioning augmentation system is stable. However, it is necessary to consider the bias. This bias is caused by the earth's crustal movement consideration, which can be neglected by the CLAS positioning augmentation system. The results verify that the bias error between the CLAS and the RTK positioning augmentation system is less than 0.10 m. The bias error between the MADOCA and the RTK positioning augmentation system is less than 0.40 m. This bias error is larger than the bias error between the CLAS and the RTK positioning augmentation system because of the big oscillation of the MADOCA positioning augmentation system caused by the time dependency of this system, as concluded from the analysis of the data shown in Figure 5.6 and Figure 5.7 and summarized in Table 5.3 and Table 5.4. These biases are also caused by the simultaneous change of position in the easting and northing coordinates while the robot combine harvester is running. The bias from the change of the position will always be visible even when the auto-guided combine harvester uses the RTK positioning augmentation system as a navigation sensor. This bias should be less notorious

if the direction of the pre-designed navigation map is parallel to one of the UTM coordinate system the northing or easting direction. However, this condition is unrealistic and cannot be implemented in practical applications. This raises the question of whether it would be possible to adjust the values obtained from the CLAS positioning augmentation system by estimating an almost constant bias in both easting and northing directions. However, this is a work still in progress and is out of the scope of this research.

5.4 Conclusion

This chapter explained the experiment methodology to test the feasibility of utilizing the QZSS as a navigation sensor for an auto-guided combine harvester. Three feasibility tests were presented. The purpose of the first test is to verify the possibility of utilization of both CLAS and MADOCA positioning augmentation systems as a navigation sensor for an auto-guided combine harvester. The purpose of the second test is to investigate the dynamic characteristic of the CLAS and MADOCA positioning augmentation system while using the RTK positioning augmentation as a navigation sensor. Finally, the purpose of the third test is to evaluate the performance of the CLAS and MADOCA positioning augmentation system as a navigation sensor for an auto-guided combine harvester.

The results from the three tests shows the similar results from Chapter 4, meaning the CLAS positioning augmentation had a better performance than the MADOCA positioning augmentation system which has a time dependency. This suggests that the MADOCA position augmentation system is not suitable for the practical application to utilize as a navigation sensor for the auto-guided combine harvester. On the other hand, the CLAS positioning augmentation system is stable and suitable to utilize for the practical application.

CHAPTER 6
RESEARCH SUMMARY

This chapter summarizes this research then highlights the most important aspects of this thesis chapter by chapter.

6.1 Introduction

Chapter 1 presented concepts concerning agricultural vehicles. It briefly explained the positioning system for an automatic combine harvester. This chapter also introduces the motivation and objectives of this research. The research background explained the problem of food shortage and the issue of the decreasing of agricultural labor. Therefore, the positioning systems or navigation systems for agricultural vehicles were researched and developed to counteract with this mentioned issue.

This research was focusing on develop a positioning system for an automatic combine harvester. With the improvement of the technologies and innovations, the evolution of automated guidance from mechanical sensing to electronic sensors, machine vision, and GNSS to successfully navigate vehicles following parallel paths through the field. From the literature review, three positioning systems for an automatic combine harvester; positioning based on machine vision, positioning based on laser rangefinder, and positioning based on GNSS; were introduced in this chapter.

Therefore, the objective of this thesis was stated as to develop a positioning system for an automatic combine harvester. To achieve this purpose, this thesis introduced three objectives. The first one is to develop a local positioning system based on crop edge detection by integrating a laser rangefinder and machine vision. The second one is to evaluate the performance of the QZSS for a combine harvester under static conditions. The third objective

is to examine the feasibility of an auto-guided combine harvester utilizing the QZSS as a navigation sensor.

To fulfill the first objective of this thesis, the Dempster-Shafer (DS) theory was used as a sensor fusion technique to integrate the data from a laser rangefinder and machine vision. To fulfil the second objective of this thesis, the Centimeter Level Augmentation Service (CLAS) and the Multi-Global Navigation Satellite System Advanced Demonstration tool for Orbit and Clock Analysis (MADOCA) positioning augmentation system, both using the signal provided by the QZSS were evaluated their performance under static conditions. Then to fulfil the third objective of this thesis, both systems were utilized as the navigation sensor for the auto-guided combine harvester to examine the feasibility.

6.2 Research platform

Chapter 2 explained the equipment used in this thesis. The research platform implemented in the Yanmar AG-1100 combine harvester used for the stimulation and field experiments is introduced including the specifications of the vehicle. For the development of a local positioning system based on crop edge detection, the test vehicle was equipped with an IMU, an RGB camera and a laser rangefinder attached to the PTU. For the development of the positioning based on GNSS, the test vehicle was equipped with two GNSS receivers, which one of them can obtain the signal from the QZSS.

The RGB camera is equipped to collect the features of the target object. A 2D laser measures the time taken by the pulse to be reflected off the target object and returned to the sensor. The PTU allows real-time movement of its payload sensors, increasing the effective field of view of such sensors. The IMU measures the inclinations of the vehicle which are roll, pitch, and yaw angle.

The QZSS is a satellite navigation system for users around Japan and Oceania developed by Japan. Comparing to the RTK positioning augmentation system, the QZSS does not require an Internet Service Provider (ISP) nor an NTRIP service provider to obtain the correction signal from the reference station. The Magellan MJ-30080-GM-QZS receiver was used to provide CLAS and MADOCA positioning augmentation systems. The Trimble-SPS855 was used to provide the RTK positioning augmentation system. The GPS Networking ALDCBS1X2 GNSS splitter was used to receive the satellite signal from a single GNSS antenna into two GNSS receivers.

6.3 Local positioning system based on crop edge detection by integrating a laser rangefinder and machine vision

Chapter 3 presented the development of the local positioning system based on crop edge detection by integrating a laser rangefinder and machine vision. To integrate both sensors, the fundamentals of sensor fusion and its theory were introduced. The concept of sensor's uncertainty and accuracy was described to specify that a sensor fusion method can be used to manipulate the uncertainty of sensor. Then, three sensor fusion theories were proposed; Bayesian probability theory, Dempster-Shafer theory, and fuzzy logic. The Dempster-Shafer theory was selected as the sensor fusion method to develop the system. This theory does not require the prior probability distribution which makes it suitable for the real-time positioning. In the real-time positioning, there is unknown prior probability distribution.

The experiments methodology was explained. The simulation experiment was performed by using card boxes simulated as crops to evaluate the accuracy of the developed system. The experiments were divided into three parts; the RGB camera detects the edge of the card boxes, Laser rangefinder detects the edge of the card boxes, and sensor fusion detects the edge of the card boxes.

Results of the developed system shows that the observation of both sensors is certainty with the probability mass for percept equal to 0.70 and the weight of conflict equal to 0.14. The probability mass for percept equal to 0.70 means the observation of the sensor fusion detection of the edge of card boxes is certain. However, it is not suitable to use the probability function for the practical application like the operation of an automatic combine harvester. Therefore, the further experiment and evaluation is necessary to develop a positioning system for an automatic combine harvester.

6.4 Performance of Quasi-Zenith Satellite Systems for a combine harvester under static conditions

Chapter 4 presented the performance evaluation while utilizing QZSS for a combine harvester under static conditions. According to the development of the QZSS and its receiver which can provide the CLAS and MADOA positioning augmentation system, both systems have a good accuracy which suggest that both can be utilized as the positioning system of an automatic combine harvester.

To evaluate the performance of the CLAS and MADOCA positioning augmentation system under static conditions the RTK positioning augmentation system was used as a reference. The experiments were conducted in an open sky area. The receiver antennas were mounted on a tripod stand using a brass plumb bob to set the tripod in the exact same central position of a selected post hole as the landmark, to guarantee that the three positioning augmentation systems in the experiment measured the exact same position.

A simple activation test was performed on each of the receivers at the experimental location. Then, an additional reactivation time test was also performed. The results showed an average activation time of around 14.2 seconds, 128.1 seconds, and 30.3 seconds for the RTK, CLAS, and MADOCA positioning augmentation systems, respectively. The average reactivation

time was around 12.9 seconds and 43.3 seconds for the RTK and MADOCA positioning augmentation systems, respectively.

To evaluate the performance under static conditions, The $2DRMS$, CEP, and $RMSE$ were calculated. The results showed a $2DRMS$ of 0.04 m and 0.10 m, a CEP of 0.03 m and 0.08 m, and a $RMSE$ of 0.57 m and 0.54 m for the CLAS and MADOCA positioning augmentation system, respectively.

6.5 Feasibility of an auto-guided combine harvester utilizing Quasi-Zenith Satellite Systems as a navigation sensor

Chapter 5 presented the tests by utilizing the CLAS and MADOCA positioning augmentation system as a navigation sensor for an auto-guided combine harvester. The tests are necessary according to the results from Chapter 4, both CLAS and MADOCA positioning augmentation systems could achieve a good performance especially, the CLAS positioning augmentation system.

Three feasibility tests were performed which had a different purpose on each test. The first test verified that the auto-guided combine harvester could perform a run along the four paths of the pre-designed navigation map while utilizing the CLAS and MADOCA positioning augmentation systems as navigation sensor.

From the second test, the CLAS positioning augmentation system achieved a performance as good as the RTK positioning augmentation system with an average $RMSE$ of the lateral deviation less than 0.06. In contrast, the MADOCA positioning augmentation system achieved a poor performance in the first run and it gradually improved in the next run meaning it might not be practical to utilize the MADOCA positioning augmentation system as a navigation sensor for an auto-guided combine harvester.

The third test confirmed that the MADOCA position augmentation system has a time dependency, and it is not suitable for the practical application. On the other hand, the CLAS positioning augmentation system is stable and suitable to utilize as a navigation sensor for an auto-guided combine harvester.

6.6 Conclusions

According to the problem of food shortage and the issue of the decreasing of agricultural labor, the positioning systems or navigation systems for agricultural vehicles were researched and developed to deal with the mentioned problems. The objective of this research was to develop positioning systems for an automatic combine harvester. The first developed system is the local positioning system based on crop edge detection by integrating a laser rangefinder and a machine vision. The second system is the positioning based on GNSS by utilizing the QZSS as a navigation sensor for an auto-guided combine harvester.

The developed local positioning system based on crop edge detection by using sensor fusion to integrate a laser rangefinder and an RGB camera showed the results with the probability mass for percept of 0.70, meaning the observation of the sensor fusion in the simulation experiments is certain. However, using the probability technique is not suitable for practical application of an automatic combine harvester because it lacks robustness.

Before utilizing the QZSS as a navigation sensor for an auto-guided combine harvester, the CLAS and MADOCA positioning augmentation systems were evaluated in terms of performance under static conditions. The availability and the accuracy were evaluated by measuring the activation time, the reconnection time, and obtaining a Twice Distance Root Mean Square (2DRMS) of 0.04 m and 0.10 m, a Circular Error Probability (CEP) of 0.03 m and 0.08 m, and a Root Mean Square Error (RMSE) of 0.57 m and 0.54 m for the CLAS and MADOCA, respectively. This mean both systems have a potential to utilize them as a navigation sensor for an auto-guided combine harvester.

The developed positioning system based on GNSS by utilizing the CLAS and MADOCA positioning augmentation systems as a navigation sensor for the auto-guided combine harvester showed that the MADOCA positioning augmentation system is not suitable for practical application due to the time dependency of this system. In contrast, the results prove that the CLAS positioning augmentation system is sufficiently good to utilize it as the navigation sensor for the auto-guided combine harvester.

List of publication

Journal papers

Udompant, K., Ospina, R., Kim, Y. J., & Noguchi, N. (2021). Utilization of Quasi-Zenith Satellite System for Navigation of a Robot Combine Harvester. *Agronomy*, *11*(3), 483.

Appendix A

DATASHEET

Trimble SPS855

GNSS MODULAR RECEIVER

FLEXIBLE RECEIVER FOR JOBSITE MEASUREMENT

Whether you need a reliable GNSS base station or a rugged rover, the Trimble® SPS855 GNSS Modular Receiver gives you the flexibility to perform all of your construction site measurements. As a permanent or semi-permanent base station, it provides GNSS corrections for site measurements and machine control. As a rover, it can move easily from a site supervisor truck to a pole mount for grade checking, site measurement and stakeout.

The versatile SPS855 receiver is available in a range of options to suit your jobsite or marine construction performance requirements. Simply purchase the receiver that you need today, and upgrade as your needs change.

Key Features

Secure and Easy to Use

The Trimble SPS855 is comprised of an integrated GNSS receiver and radio plus a choice of external antenna. The receiver can be placed in a secure environment such as the job trailer or boat cabin where it is protected from theft and weather. The less expensive antenna can be placed in a location with clear visibility to the sky and maximum radio coverage.

You don't have to be a GNSS expert to use the SPS855. Integrated 450 or 900 MHz license-free radio and interface with Trimble Siteworks Software to make the SPS855 easy to use, fast to setup and more productive on the job. Trimble Autobase™ technology means anyone on the jobsite can perform daily base station set up with one button push.

For more advanced troubleshooting, the receiver's web interface allows your GNSS manager to remotely monitor base station performance, availability, and configuration. No need for time-consuming and costly visits to the base station to set up each day or diagnose issues that may arise.

The fully upgradable SPS855 GNSS Modular Receiver can be configured in a variety of ways. For example:

- As a base station only
- As a rover only with SBAS, Location, or Precision Real-Time Kinematic (RTK) accuracy
- As a flexible base or rover with Precision RTK accuracy

The SPS855 can be combined with the Trimble SPS555H Heading Add-on Receiver, for applications on cranes, construction vessels, and dredges where real-time position and orientation are important.

DATASHEET

Trimble SPS855 GNSS MODULAR RECEIVER

GENERAL

Keyboard and display: Vacuum fluorescent display 16 characters by 2 rows
Dimmable. On/Off key for one-button startup
Dimensions (L × W × D): 24 cm × 12 cm × 5 cm (9.4 in x 4.7 in x 1.9 in)
Weight: 1.65 kg (3.64 lb) receiver with internal battery and radio
1.55 kg (3.42 lb) receiver with internal battery and no radio

ANTENNA OPTIONS

Zephyr™ 2 Models: Triple frequency GNSS (GPS, GLONASS, Galileo, BeiDou), MSS (CenterPoint RTX, OmniSTAR™, L1 SBAS)
GA830: Triple frequency GNSS (GPS, GLONASS, Galileo, BeiDou), MSS (CenterPoint RTX, OmniSTAR, L1 SBAS)
GA530: L1/L2/L2C GPS, SBAS, RTX and OmniSTAR

ENVIRONMENT

Operating[1]: –40 °C to +65 °C (–40 °F to +149 °F)
Storage: –40 °C to +80 °C (–40 °F to +176 °F)
Humidity: MIL-STD 810F, Method 507.4
Waterproof: IP67 for submersion to depth of 1 m (3.3 ft), dust proof
Pole drop: Designed to survive a 1 m (3.3 ft) pole drop onto a hard surface

MEASUREMENTS[2]

- 440-channel L1C/A, L1/L2/L2C GPS and QZSS.
- Upgradable to L5 and GLONASS L1/L2C/A, L1/L2P Full Cycle Carrier
- Galileo
- BeiDou
- CenterPoint™ RTX™ Correction Service
- OmniSTAR
- Trimble EVEREST™ multipath signal rejection
- 4-channel SBAS (WAAS/EGNOS/MSAS/QZSS)

CODE DIFFERENTIAL GPS POSITIONING[3]

Horizontal accuracy: 0.25 m + 1 ppm RMS (0.8 ft + 1 ppm RMS)
Vertical accuracy: 0.50 m + 1 ppm RMS (1.6 ft + 1 ppm RMS)

REAL-TIME KINEMATIC (RTK UP TO 30 KM) POSITIONING[4]

Horizontal accuracy: 8 mm + 1 ppm RMS (0.026 ft + 1 ppm RMS)
Vertical accuracy: 15 mm + 1 ppm RMS (0.05 ft + 1 ppm RMS)

TRIMBLE XFILL

Horizontal accuracy: RTK4 +10 mm/minute RMS
Vertical accuracy: RTK +20 mm/minute RMS

TRIMBLE CENTERPOINT RTX

Horizontal accuracy: 4 cm (0.13 ft) RMS
Vertical accuracy: 9 cm (0.30 ft) RMS

INITIALIZATION TIME

Initialization reliability[5]: > 99.9%

OPERATION TIME ON INTERNAL BATTERY

Rover: 13 hours; varies with temperature
Base station
- 450 MHz systems: Approximately 11 hours; varies with temperature[6]
- 900 MHz systems: Approximately 9 hours; varies with temperature
- 220 MHz systems: Approximately 9 hours; varies with temperature

POWER

Internal: Integrated internal battery 7.2 V, 7800 mA-hr, Lithium-ion
External: Power input on 7-pin 0-shell Lemo connector is optimized for lead acid batteries with a cut-off threshold of 11.5 V
Power input on the 26-pin D-sub connector is optimized for Trimble Lithium-ion battery input with a cut-off threshold of 10.5 V
Power consumption: 6.0 W in rover mode with internal receive radio
8.0 W in base mode with internal transmit radio

REGULATORY APPROVALS

- FCC: Part 15 Subpart B (Class B Device) and Subpart C, Part 90
- Canadian ICES-003. Cet appareil numérique de la classe B est conforme à la norme NMB-003 du Canada.
- Canadian RSS-310, RSS-210, and RSS-119. Cet appareil est conforme à la norme CNR-310, CNR-210, et CNR-119 du Canada.
- ACMA: AS/NZS 4295 approval
- CE mark compliance
- C-tick mark compliance
- UN ST/SG/AC.10.11/Rev. 3, Amend. 1 (Lithium-ion Battery)
- UN ST/SG/AC.10/27/Add. 2 (Lithium-ion Battery)
- RoHS compliant
- WEEE compliant
- China CRRC - 220 MHz

COMMUNICATIONS

Lemo (Serial): 7-pin 0 S Lemo, Serial 1, 3-wire RS-232
Modem 1 (Serial): 26-pin D-sub, Serial 2, Full 9-wire RS232, using adaptor cable
Modem 2 (Serial): 26-pin D-sub, Serial 3, 3 wire RS-232, using adaptor cable
1PPS (1 Pulse-per-second): Available on Marine versions
Ethernet: Through a multi-port adaptor
Bluetooth wireless technology: Fully-integrated, fully-sealed 2.4 GHz Bluetooth module[7]
Integrated radios (optional): Fully-integrated, fully-sealed
Internal 450 MHz (UHF) Tx/Rx;
Internal 900 MHz Tx/Rx;
Internal 220 MHz Tx/Rx
External GSM/GPRS, cell phone support: For Internet-based correction streams
Receiver position update rate: 1 Hz, 2 Hz, 5 Hz, 10 Hz, and 20 Hz positioning
Correction data input/output: CMR™, CMR +™, CMRx, RTCM v 2.x & 3.x
Data outputs: NMEA, GSOF, 1PPS Time Tags (Marine version)

1 Receiver will operate normally to –40 °C. The internal battery will operate from –20° C to +50 ° C. All temperatures listed are ambient.
2 The Trimble SPS855 GNSS Modular Receiver is capable of supporting existing and planned GNSS satellite signals, including GPS, GLONASS, Galileo, CenterPoint RTX, Quasi Zenith Satellite System and BeiDou, and existing and planned augmentations to these GNSS systems. Support for the Galileo system is developed under a license of the European Union and the European Space Agency.
3 Accuracy and reliability may be subject to anomalies such as multipath, obstructions, satellite geometry, and atmospheric conditions. Always follow recommended practices.
4 RTK refers to the last reported precision before the correction source was lost and xFill started.
5 May be affected by atmospheric conditions, signal multipath, and satellite geometry. Initialization reliability is continuously monitored to ensure highest quality.
6 For receivers with the 2.0 Wupgrade, reduced battery performance should be expected compared to the 0.5W solution.
7 Bluetooth type approvals are country specific. For more information, contact your local Trimble office or representative.

Specifications subject to change without notice.

TRIMBLE CIVIL CONSTRUCTION
10368 Westmoor Drive
Westminster CO 80021 USA
800-361-1249 (Toll Free)
+1-937-245-5154 Phone
construction_news@trimble.com

Appendix B

ALDCBS1X2

GPS Amplified 1X2 Splitter Technical Product Data

Features

- Excellent Gain Flatness
  - Less than 1 dB variation between ports.
- Flat Group Delay
  - Less than 1ns variation between L1 and L2.
- High Output Gain
  - 22 dB gain is typical across all operating frequencies.
- Wide Accepted Frequency Range
  - Accepts signals from the entire L-Band, covering all major GNSS constellations.
- Efficiently Blocked Ports
  - Uses 200Ω resistors to prevent antenna alarm faults from connected devices.
- Matched Phase Balance
  - Less than 1° of variation between ports.

Description

This Amplified Loaded DC Blocked **S**plitter **1X2 (ALDCBS1X2)** is an active one input, two output splitter that splits signals from 1.1 GHz to 1.7 GHz. This equipment is designed to amplify and split signals within the L-band to provide two devices with the signal from a single antenna. In the standard configuration, the J1 port will pass DC voltage from a connected device and pass this power to the antenna or other devices upline from the splitter via the antenna port. The other port (J2) is DC blocked and loaded with 200Ω resistors to simulate antenna current draw which prevents antenna alarm faults. Custom gain, DC power, and connector configurations are available upon request.

Use Cases

- Splitting and amplifying a roof antenna signal between 2 GPS/GLONASS/GNSS receivers.
- Splitting and amplifying WAAS antenna between WASS receiver and ADS-B.
- Splitting and amplifying an antenna signal to 2 passive antennas to re-radiate 2 spaces.
- Usable as a small part of a larger signal distribution network.

ALDCBS1X2

Electrical Specifications, TA=25°C

General Specification

Parameter	Notes	Min	Typ	Max	Unit
Frequency Range	Covers all major GNSS constellations.	1.1		1.7	GHz
Characteristic Impedance	Unused ports should be terminated with 50Ω loads.		50		Ω
Req. DC Input V.	Operating Voltage Range.	3.3		15	VDC
Input P1dB	The 1dB compression point.		-24		dBm
Current Draw(1)	Typical current consumption.			23	mA

GPS L1 & L2 RF Specification

Parameter	Notes	Min	Typ	Max	Unit
Gain	The relative increase in signal power provided by the amplifier.	21	22	23.5	dB
Input SWR	Input Standing Wave Ratio: S11			2.0:1	-
Output SWR	Output Standing Wave Ratio: S22			1.8:1	-
L1 Noise Figure	The increase in noise power relative to an ideal amplifier.		2.5	3.25	dB
Gain Flatness	The difference in loss or gain between the L1 and L2 frequencies.		0.5	1	dB
Amplitude Balance	The difference in gain or loss between each output port.			1.0	dB
Phase Balance	The difference in phase variation between each output port.			1.0	deg
Isolation	The amount of attenuation between two output ports.	L2:15 L1:22			dB
Group delay flatness	The difference in signal delay between the L1 and L2 frequencies.			1	ns
Input P1dB	The 1dB compression point.		-24		dBm
Current Draw	Typical current consumption.			23	mA

External Power Options (Networked Option)		
Source Voltage Options	Voltage Input	Style
	110VAC	Transformer (ITA Type A Wall Mount)
	220VAC	Transformer (ITA Type C Wall Mount)
	240VAC (United Kingdom)	Transformer (ITA Type G Wall Mount)
	Customer Supplied DC 9-32 VDC	Mil DC Connector (Includes Mate)
Output Voltage Options (1)	DC Voltage Out	Max Current out For Corresponding Vout
	3.3 V	110mA
	5V	130mA
	9V	140mA
	12V	180mA
	15V	220mA
	Custom	Custom
Standard DC Configuration without External Power Option		
J1/Output 1 Pass DC, J2/Output 2 Block DC, Input Pass DC		
Standard DC Configuration with any External Power Option (AC/DC or Military DC)		
All Outputs DC Blocked with 200Ω load standard		
Any port can be custom selected to Pass or Block DC		
Connector Options	Connector Style	Charge
	Type N-female	No Charge
	Type SMA-female	No Charge
	Type TNC-female	No Charge
	Type BNC-female	No Charge
	Other	Contact GPS Networking

(1)With Network Option, any RF port (input or output) can be specified to Pass DC or Block DC

For sales or technical support contact us at 1-800-463-3063 or salestech@gpsnetworking.com

ALDCBS1X2

Part Number Configuration

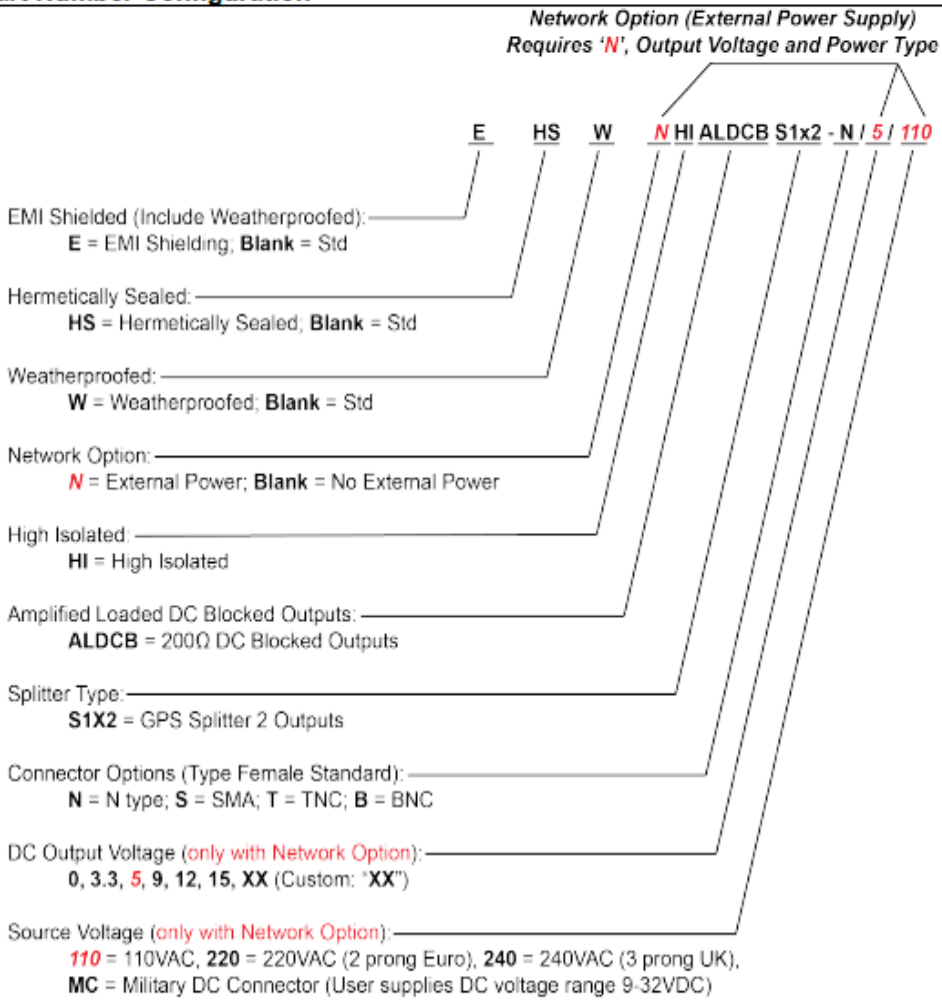

(Military DC Mating Connector is included standard with the MC power option).

When no external power supply option (AC or DC) is selected, Output 1/J1 is Pass DC Standard.
When external power supply option is selected, all outputs are DC blocked standard.

Contact GPS Networking Technical Support at 1-800-463-3063 or salestech@gpsnetworking.com for any questions regarding non-standard configurations and corresponding part numbers.

ALDCBS1X2

Performance

ALDCBS1X2 (Standard Gain, typical)

Each ALDCBS1X2 ships with a test sheet that verifies critical performance characteristics, such as gain, input VSWR, and amplitude balance; a typical VNA test sheet is shown below.

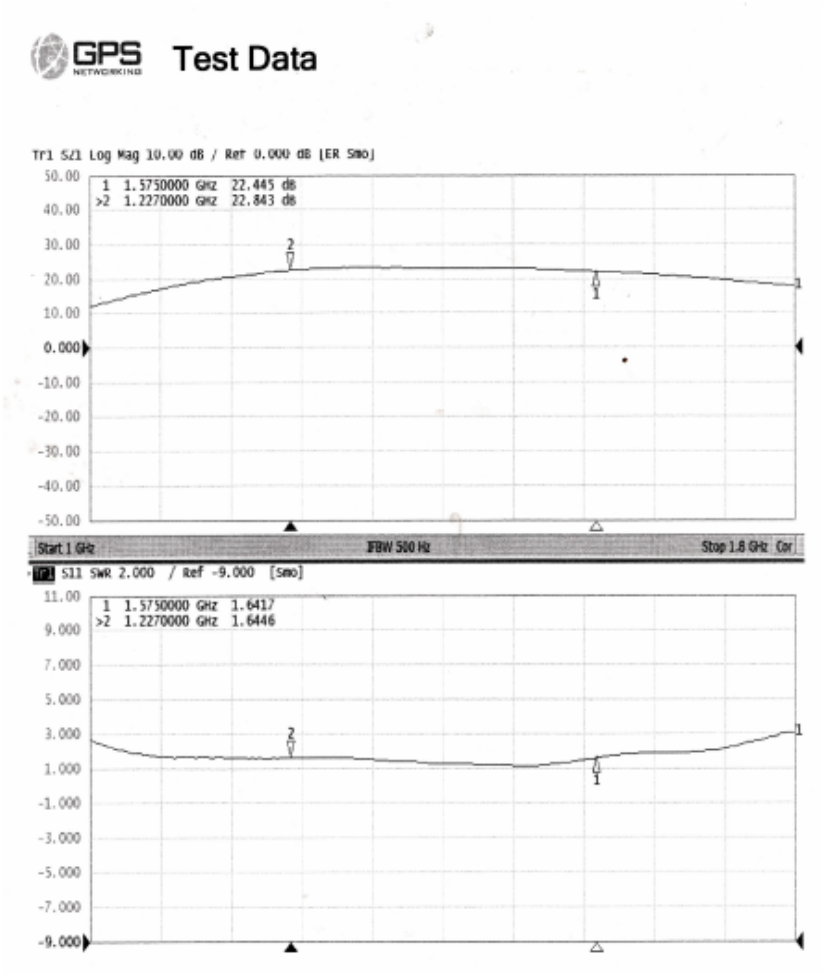

Mechanical

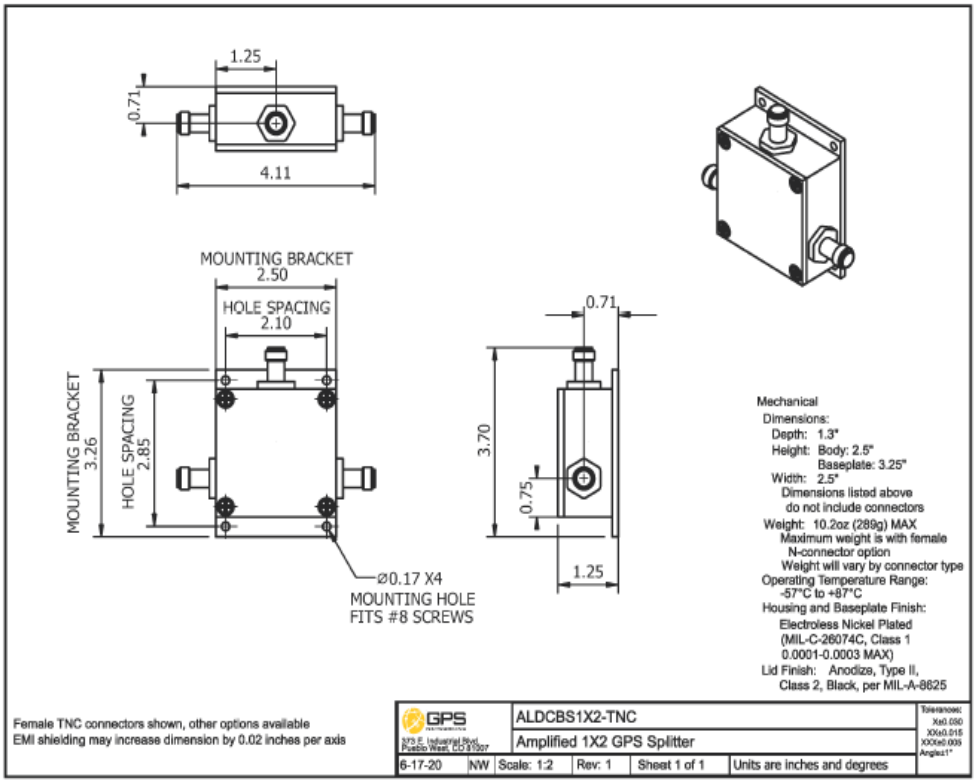

Contact us at salestech@gpsnetworking.com for 3D models or CAD drawings.

References

Barawid, O. C. (2010). Development of electronic utility robot vehicle (Doctoral dissertation, PhD thesis. Graduation School of Agriculture, Hokkaido University, Sapporo, Japan).

Bell, T. (2000). Automatic tractor guidance using carrier-phase differential GPS. *Computers and electronics in agriculture*, *25*(1-2), 53-66.

Brooks, R. R., & Iyengar, S. S. (1998). *Multi-sensor fusion: fundamentals and applications with software*. Prentice-Hall, Inc..

Castleden, N., Hu, G. R., Abbey, D. A., Weihing, D., Øvstedal, O., Earls, C. J., & Featherstone, W. E. (2004). First results from virtual reference station (VRS) and precise point positioning (PPP) GPS research at the western Australian Centre for Geodesy. *Journal of Global Positioning Systems*, *3*(1-2), 79-84.

Chateau, T., Debain, C., Collange, F., Trassoudaine, L., & Alizon, J. (2000). Automatic guidance of agricultural vehicles using a laser sensor. *Computers and electronics in agriculture*, *28*(3), 243-257.

Cho, W., Iida, M., Suguri, M., Masuda, R., & Kurita, H. (2014). Using multiple sensors to detect uncut crop edges for autonomous guidance systems of head-feeding combine harvesters. *Engineering in Agriculture, Environment and Food*, *7*(3), 115-121.

Cho, W., Iida, M., Suguri, M., Masuda, R., & Kurita, H. (2014). Vision-based uncut crop edge detection for automated guidance of head-feeding combine. *Engineering in Agriculture, Environment and Food*, *7*(2), 97-102.

Choi Jongmin. (2014). Development of Guidance System Using Local Sensors for Agricultural Vehicles. (Doctoral dissertation, PhD thesis. Graduation School of Agriculture, Hokkaido University, Sapporo, Japan).

Choy, S., Harima, K., Li, Y., Choudhury, M., Rizos, C., Wakabayashi, Y., & Kogure, S. (2015). GPS precise point positioning with the Japanese Quasi-Zenith Satellite System LEX augmentation corrections. *The Journal of Navigation*, *68*(4), 769-783.

Choy, S., Bisnath, S., & Rizos, C. (2017). Uncovering common misconceptions in GNSS Precise Point Positioning and its future prospect. *GPS solutions*, *21*(1), 13-22.

Drosos, V. K., Malesios, C., & Soutsas, K. P. (2011). Planimetry reliability with GPS. In *Pushing the boundaries with research and innovation in forest engineering. FORMEC 2011, Proceedings of the 44th International Symposium on Forestry Mechanisation, Graz, Austria, 9-13 October 2011*. Institute of Forest Engineering, University of Natural Resources and Life Sciences.

Fan, P., Li, W., Cui, X., & Lu, M. (2019). Precise and robust RTK-GNSS positioning in urban environments with dual-antenna configuration. *Sensors*, *19*(16), 3586.

Fehr, B. W., & Gerrish, J. B. (1995). Vision-guided row-crop follower. *Applied engineering in agriculture*.

Fotopoulos, G., & Cannon, M. E. (2001). An overview of multi-reference station methods for cm-level positioning. *GPS solutions*, *4*(3), 1-10.

Iida, M., Ikemura, Y., Suguri, M., & Masuda, R. (2010). Cut-edge and Stubble Detection for Auto-Steering System of Combine Harvester using Machine Vision. *IFAC Proceedings Volumes*, *43*(26), 145-150.

Inaba, N., Matsumoto, A., Hase, H., Kogure, S., Sawabe, M., & Terada, K. (2009). Design concept of quasi zenith satellite system. *Acta Astronautica*, *65*(7-8), 1068-1075.

Kobayashi, K. (2020, March 27). QZSS PPP Service. https://home.csis.u-tokyo.ac.jp/~dinesh/GNSS_Train_files/202001/LectureNotes/Kobayashi/2020AIT_MADOCACLAS.pdf

Lachapelle, G., Alves, P., Fortes, L. P., Cannon, M. E., & Townsend, B. (2000, September). DGPS RTK positioning using a reference network. In *Proceedings of the 13th International*

Technical Meeting of the Satellite Division of The Institute of Navigation (ION GPS 2000) (pp. 1165-1171).

Murphy, R. R. (1998). Dempster-Shafer theory for sensor fusion in autonomous mobile robots. *IEEE Transactions on Robotics and Automation*, *14*(2), 197-206.

Miya, M., Fujita, S., Sato, Y., Ota, K., Hirokawa, R., & Takiguchi, J. (2016, September). Centimeter Level Augmentation Service (CLAS) in Japanese Quasi-Zenith Satellite System, its User Interface, Detailed Design, and Plan. In *Proceedings of the 29th International Technical Meeting of the Satellite Division of The Institute of Navigation (ION GNSS+ 2016)* (pp. 2864-2869).

Noguchi, N., Reid, J. F., Will, J., Benson, E. R., & Stombaugh, T. S. (1998). Vehicle automation system based on multi-sensor integration. *ASAE paper*, *983111*.

Olshausen, B. A. (2004). Bayesian probability theory. *The Redwood Center for Theoretical Neuroscience, Helen Wills Neuroscience Institute at the University of California at Berkeley, Berkeley, CA.*

Petrovski, I. G., & Tsujii, T. (2012). *Digital satellite navigation and geophysics: A practical guide with GNSS signal simulator and receiver laboratory*. Cambridge University Press.

Rodríguez Pérez, J. R., Álvarez Taboada, M. F., Sanz Ablanedo, E., & Gavela, A. (2006). Comparison of GPS receiver accuracy and precision in forest environments. Practical recommendations regarding methods and receiver selection.

Saito, M., Sato, Y., Miya, M., Shima, M., Omura, Y., Takiguchi, J., & Asari, K. (2011, September). Centimeter-class augmentation system utilizing Quasi-Zenith Satellite. In *Proceedings of the 24th International Technical Meeting of The Satellite Division of the Institute of Navigation (ION GNSS 2011)* (pp. 1243-1253).

Searcy, S. W., & Reid, J. F. (1986, June). Vision-Based Guidance of an Agricultural Tractor. In *American Control Conference, 1986* (pp. 931-937). IEEE.

Seigo, F., Masakazu, M., & Junichi, T. (2015). Establishment of Centimeter-class Augmentation System utilizing Quasi-Zenith Satellite System. *Syst. Contr. Inf., 59*, 126-131.

Stombaugh, T. S., Benson, E. R., & Hummel, J. W. (1998). Automatic guidance of agricultural vehicles at high field speeds. *ASAE paper*, *983110*.

Teng, Z., Noguchi, N., Liangliang, Y., Ishii, K., & Jun, C. (2016). Development of uncut crop edge detection system based on laser rangefinder for combine harvesters. *International Journal of Agricultural and Biological Engineering*, *9*(2), 21-28.

Udompant, K., Ospina, R., Kim, Y. J., & Noguchi, N. (2021). Utilization of Quasi-Zenith Satellite System for Navigation of a Robot Combine Harvester. *Agronomy*, *11*(3), 483.

Wabbena, G., Schmitz, M., & Bagge, A. (2005, September). PPP-RTK: precise point positioning using state-space representation in RTK networks. In *Proceedings of the 18th International Technical Meeting of the Satellite Division of The Institute of Navigation (ION GNSS 2005)* (pp. 2584-2594).

Walpersdorf, A., Pinget, L., Vernant, P., Sue, C., Deprez, A., & RENAG team. (2018). Does long-term GPS in the Western Alps finally confirm earthquake mechanisms?. *Tectonics*, *37*(10), 3721-3737.

Wang, H., & Noguchi, N. (2019). Navigation of a robot tractor using the centimeter level augmentation information via Quasi-Zenith Satellite System. *Engineering in Agriculture, Environment and Food*, *12*(4), 414-419.

Woebbecke, D. M., Meyer, G. E., Von Bargen, K., & Mortensen, D. A. (1995). Color indices for weed identification under various soil, residue, and lighting conditions. *Transactions of the ASAE*, *38*(1), 259-269.

Yanmar Combine Harvester. (2020, March 25). Steering System Full Time Drive System. https://www.yanmar.com/global/about/technology/technical_review/2015/0401_2.html

Yin, X. (2013). *Development of in field transportation robot vehicle using multiple sensors* (Doctoral dissertation, PhD thesis. Graduation School of Agriculture, Hokkaido University, Sapporo, Japan).

Zhang, Z. (2014). *Development of a Robot Combine Harvester Based on GNSS* (Doctoral dissertation, PhD thesis. Graduation School of Agriculture, Hokkaido University, Sapporo, Japan).

Zhang, S., Du, S., Li, W., & Wang, G. (2019). Evaluation of the GPS precise orbit and clock corrections from MADOCA real-time products. *Sensors*, *19*(11), 2580.